Kinematics of Cenozoic shortening of the Hotan anticline along the northwestern margin of the Tibetan Plateau (Western Kunlun, China)

Guillaume Baby, Martine Simoes, Laurie Barrier, Christelle Guilbaud, Haibing Li, Jérôme Woerd

Kinematics of Cenozoic shortening of the Hotan anticline along the northwestern margin of the Tibetan Plateau (Western Kunlun, China)

Guillaume Baby [(1)], Martine Simoes [(1)], Laurie Barrier [(1)], Christelle Guilbaud [(1)], Haibing Li [(2)], Jérôme Van der Woerd [(3)]

(1) Université de Paris, Institut de physique du globe de Paris, CNRS, F-75005, Paris, France

(2) Institute of Geology, Chinese Academy of Geological Sciences, Beijing, China

(3) Institut Terre et Environnement de Strasbourg, Université de Strasbourg, CNRS, UMR 7063, Strasbourg, France

Corresponding author: Guillaume Baby (baby.guillaume@gmail.com)

Key Words

Balanced cross-sections, growth strata, kinematics, seismic profiles, Western Kunlun, Tarim Basin

Key Points

- Four new balanced cross-sections across the Hotan anticline (foothills of the Western Kunlun, China)
- Measured amount of shortening ranges from ~40 km to ~34.5 km, and deformation probably initiated by ~16 Ma
- Growth strata analysis points to a decrease in shortening rates since ~8-9 Ma, probably related to a regional kinematic reorganization

Abstract

Kinematic constraints on the Cenozoic deformation along the northwestern edge of the Tibetan Plateau remain limited. Combining surface geological data and seismic profiles, we document the structural geometry and kinematics of the large-scale east-west striking Hotan anticline, along the foothills of the Western Kunlun Range. Four new balanced cross-sections are constructed, and the temporal evolution of deformation is deciphered from the exceptionally well-imaged growth strata at the front of the fold. This anticline results from a broad fault-bend fold, subsequently deformed by a footwall duplex. The total shortening across the whole structure is relatively constant along strike, from ~40 to ~35 km. However, the shortening accommodated by the duplex varies laterally from ~50-40 % to 0 % of the total shortening. Two distinct successive patterns of growth strata are recognised and are interpreted to be representative of deformation on the ramp anticline, followed by deformation on the duplex. The onset of deformation initiated by ~16 Ma. Deformation of the underlying duplex began at ~12 Ma to the west and subsequently propagated eastward. From these results, we determine a shortening rate of ~5 mm/yr from ~16 to ~8-9 Ma across the Hotan thrust system, followed by a significant decrease in shortening rate, possibly down to <0.5 mm/yr. We explore the significance of this deceleration of deformation at the scale of the Western Kunlun foothills and at a broader regional scale as it may point to a regional kinematic re-organisation by the late Miocene.

1. Introduction

The Cenozoic Indo-Asian collision resulted in the formation of the modern Tibetan Plateau [e.g., *Allègre et al.*, 1984; *Kapp and DeCelles*, 2019]. This geologic and topographic feature is

exceptional in that it has for long been used as a natural case example to better understand the mechanics of the continental lithosphere, with two main end-member models of continental deformation [e.g., *England and Houseman*, 1989; *Tapponnier et al.*, 2001]. Whether deformation has been localized or distributed, the contribution of major structures or structural ensembles to deformation, as well as the timing and kinematics of deformation at the continental scale, are key observations to move forward in our understanding of how the continental lithosphere deforms. Numerous studies have focused on major strike-slip faults surrounding the Tibetan Plateau, such as the Altyn-Tagh [e.g., *Mériaux et al.*, 2004; *P Z Zhang et al.*, 2007] or the Karakoram [e.g., *Phillips and Searle*, 2007; *Valli et al.*, 2008] faults, or on the mountain range bordering the eastern part of the Plateau, such as the Long Men Shan [e.g., *Hubbard and Shaw*, 2009; *Royden et al.*, 1997]. Comparatively, the compressive structures along the northwestern margin of the Plateau have been much less investigated. Here, we aim at further documenting the deformation of this margin corresponding to the Western Kunlun Range **(Figure 1)**, in order to move forward in our knowledge of the kinematics of deformation of this part of the collision zone.

The Western Kunlun Range (hereafter WKR) propagated northwards since the late Oligocene in response to the Indo-Asian collision that reactivated Paleozoic and Mesozoic compressive structures [e.g., *Cao et al.*, 2015; *G Li et al.*, 2019; *Matte et al.*, 1996]. Balanced cross-sections indicate that a large part of the total shortening across this range was accommodated by thin-skinned tectonics within its foothills, with structures propagating into the southwestern Tarim Basin [*Laborde et al.*, 2019 and references therein] **(Figures 1.C and 1.D)**. Despite a growing number of studies documenting the deep structure of this outer part of the WKR from seismic profiles [e.g., *Cheng et al.*, 2017; *X-D Jiang et al.*, 2013; *Li et*

66 *al.*, 2021; *Lu et al.*, 2016; *T Sun et al.*, 2019; *C Wang et al.*, 2016; *S Wang et al.*, 2021],
67 quantitative constraints are still missing to document the long-term temporal evolution of
68 deformation in this region.

69 Syn-tectonic sedimentary layers - commonly called growth strata - are key to interpret and
70 quantify the long-term kinematics of fold-thrust structures [e.g., *Ford et al.*, 1997;
71 *Medwedeff*, 1989; *Poblet et al.*, 2004; *Riba*, 1976; *Suppe et al.*, 1992]. However, the study of
72 growth strata remains often challenging, as it largely depends on the degree of preservation
73 and exposure of these layers [e.g., *Vergés et al.*, 2002], and on the possibility of dating
74 them. Numerous studies, for example within the foothills of the Pamir or of the southern
75 Tian Shan ranges [e.g., *Charreau et al.*, 2006; *Charreau et al.*, 2020; *Charreau et al.*, 2009; *J*
76 *Chen et al.*, 2002; *Heermance et al.*, 2007; *Heermance et al.*, 2008; *Huang et al.*, 2010;
77 *Huang et al.*, 2006; *Hubert-Ferrari et al.*, 2007; *C Li et al.*, 2019; *J Sun et al.*, 2009; *Thompson*
78 *et al.*, 2015; *Thompson Jobe et al.*, 2018; *T Zhang et al.*, 2014], have successfully exploited
79 such syn-tectonic record to quantify the kinematics of folding and thrusting. This is not
80 much the case for the foothills of the WKR as structures remain most often buried beneath
81 the sedimentation level of the Tarim foreland, so that growth layers are in most cases not
82 exposed. The existence of a large seismic dataset within the Tarim Basin provides, however,
83 opportunities to explore this buried record of the kinematics of deformation in this region.

84 Here, we investigate the Hotan anticline, which appears as a prominent structure along the
85 WKR foothills **(Figure 1.C)**. It has been previously interpreted as a simple fault-bend fold
86 [*Cheng et al.*, 2017; *X-D Jiang et al.*, 2013], but new available seismic data show a more
87 complex structure, characterized by lateral structural variations related to a blind duplex,
88 and a rich but yet-to-be-explored set of growth strata at its front. To further analyse the

89 complex geometry and kinematics of the Hotan anticline, together with its lateral variations,
90 four balanced cross-sections are presented and the kinematic evolution is deciphered from
91 the seismic profiles where the growth strata are exceptionally well-imaged. By combining
92 our estimate of shortening and timing of deformation, we find that deformation initiated
93 sometime by ~16 Ma and significantly slowed down by ~8-9 Ma. Finally, we discuss our
94 findings and their possible inferences at a regional scale.

95 ## 2. Geological context

96 ### *2.1. General setting*

97 The WKR forms a ~700 km-long curved orogenic wedge that separates the Pamir Mountains
98 to the west and the Tibetan Plateau to the south from the Tarim Basin to the northeast
99 **(Figures 1.A.B)**. Here, we focus on the east-west-striking segment of the range extending
100 between the cities of Yecheng and Hotan **(Figure 1.C)**. This segment is bounded by the
101 Karakax dextral fault to the south and faces the underthrusting Tarim foreland basin to the
102 north. This part of the belt has a length of ~350 km and a width of ~140 km, with altitudes
103 up to ~6400 m in the hinterland, ~4000-5000 m higher than the average elevation of the
104 adjacent Tarim Basin. It also has the specificity of having a present-day deformation front
105 deported far north into this basin, ~200 km away from the topographic mountain front [e.g.,
106 *Guilbaud et al.*, 2017; *Laborde et al.*, 2019; *Lu et al.*, 2016; *Wittlinger et al.*, 2004; *Xu et al.*,
107 2020] **(Figure 1.D)**.

108 ### *2.2. Tectonic and structural framework*

The present-day orogenic wedge of the WKR results from the crustal thickening associated with the underthrusting of the Tarim Basin beneath the northwestern part of the Tibetan Plateau [*Avouac and Peltzer*, 1993; *X-D Jiang et al.*, 2013; *Laborde et al.*, 2019; *Lyon-Caen and Molnar*, 1984; *Matte et al.*, 1996; *Wittlinger et al.*, 2004]. This wedge is interpreted to rise over a basal detachment that shallows up northwards, from a middle crustal detachment below the inner range, upward into two main detachment levels within the sedimentary layers of the Tarim Basin below the foothills and the foreland of the range [e.g., *Cowgill et al.*, 2003; *Laborde et al.*, 2019; *Matte et al.*, 1996; *Wittlinger et al.*, 2004]: a relatively deep one within the middle to upper Cambrian series and a shallow one at the base of the Cenozoic deposits **(Figures 1.D and 2)**.

The inner part of the WKR results from the imbrication and exhumation of a crystalline basement and Paleozoic meta-sediments, whereas the foothills involve folded Paleozoic, Mesozoic, and Cenozoic sediments **(Figure 2)**. Five major anticlines are recognised in this outer part of the range, from west to east: the Yecheng-Pishan, Kekeya, Fusha, Pusikai and Hotan anticlines **(Figure 1.C)**. They mainly correspond to blind imbricated thrusts and duplex structures [e.g., *Guilbaud et al.*, 2017; *Laborde et al.*, 2019; *Li et al.*, 2021; *T Sun et al.*, 2019; *C Wang et al.*, 2016; *S Wang et al.*, 2021], as well as to one large blind ramp anticline known as the Hotan anticline [*Cheng et al.*, 2017; *X-D Jiang et al.*, 2013]. These structures develop where the shortening is transferred upward from the lower detachment in the middle to upper Cambrian series to the shallowest one at the base of the Cenozoic Tarim strata. Several authors suggested that the slip accommodated by these structures is transferred forward towards the foreland on this upper detachment. Such deformation could then be accommodated by the emergent Mazar Tagh thrust, ~200 km further north from the

topographic front of the WKR **(Figure 1.D)** [e.g., *H Chen et al.*, 2022; *Guilbaud et al.*, 2017; *Laborde et al.*, 2019; *Lu et al.*, 2016; *Wittlinger et al.*, 2004; *Xu et al.*, 2020].

The orogenic wedge of the WKR was formed by the reactivation of structures inherited from a previous complex geodynamic evolution [e.g., *Cao et al.*, 2015; *G Li et al.*, 2019; *Sobel and Dumitru*, 1997; *E Wang et al.*, 2003]. Different studies date this reactivation between the end of the Oligocene and the Lower Miocene: ~20 Ma as deduced from the onset of exhumation of the inner basement rocks constrained by low-temperature thermochronology [e.g., *Cheng et al.*, 2017; *G Li et al.*, 2019; *Sobel and Dumitru*, 1997; *E Wang et al.*, 2003], ~22-15 Ma from the initiation of the upward coarsening sedimentation sequence dated by magnetostratigraphy [*Blayney et al.*, 2019; *Zheng et al.*, 2015],~23-15 Ma from seismic stratigraphy and fossil record [*Cheng et al.*, 2017; *X-D Jiang and Li*, 2014], and ~16 Ma from increasing sedimentation rates in the foreland [*Métivier and Gaudemer*, 1997]. Based on a crustal budget approach, *Laborde et al.* [2019] estimate a total crustal Cenozoic shortening of 78 ± 23 km across the WKR, with ~40% of the deformation absorbed across the foothills. Using an age of 22 Ma for the onset of reactivation, this implies an average long-term shortening rate of ~3.5 mm/yr across the whole range and of ~1.5 mm/yr for the foothills. Other estimates of shortening rates over shorter time periods, from growth strata and local dated geomorphic markers along the Yecheng-Pishan anticline **(Figure 1.C)**, suggest a slip rate of 2-2.5 mm/yr, since ~5-7 Ma [*Guilbaud et al.*, 2017].

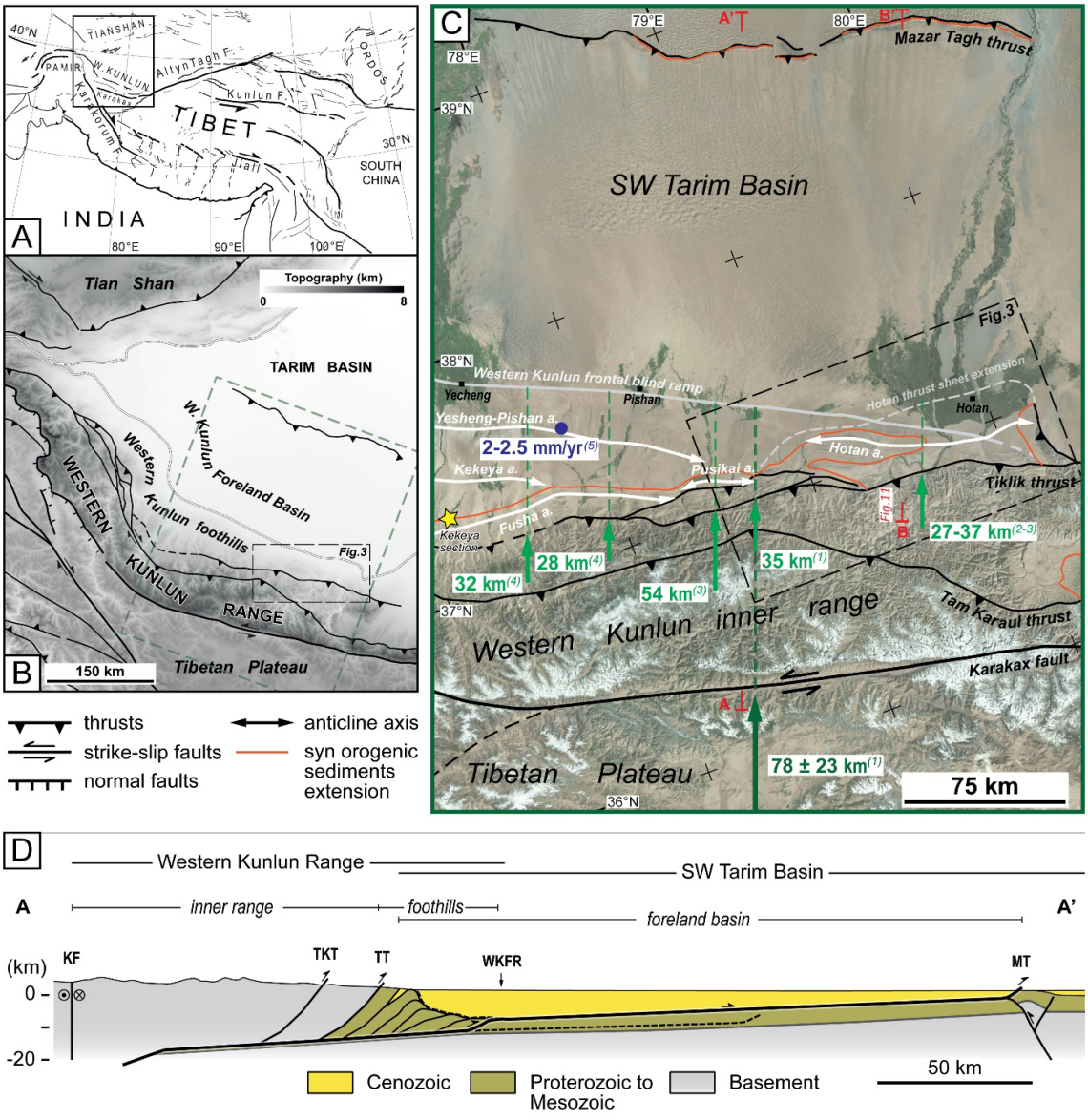

151

152 ***Figure 1:*** *Structural and tectonic setting of the study area. A. Regional tectonic map of the*

153 *Indo-Asia collision zone after [Tapponnier and Molnar, 1977]. Frame locates* ***Figure 1.B****. B.*

154 *Simplified tectonic map of the western portion of the Tarim Basin and surrounding ranges.*

155 *Elevation data are from NASA Shuttle Radar Topography Mission (3arc-second resolution)*

156 *[Jarvis et al., 2008] and the structural framework is modified from [Laborde et al., 2019].*

157 *Dashed frames locate* ***Figure 1.C*** *(large green frame) and* ***Figure 3*** *(smaller frame). C.*

158 *Tectonic map of the study area showing the main faults and the different tectonic domains*

that compose the Western Kunlun Range, modified from [Guilbaud et al., 2017]. Green arrows and values at their end report the Cenozoic shortening estimated along published cross-sections (dashed green lines), from [1][Laborde et al., 2019]; [2] [Cheng et al., 2017]; [3][X-D Jiang et al., 2013]; [4][T Sun et al., 2019]. These sections represent the deformation across the foothills (i.e. north of the Tiklik thrust). A crustal-scale shortening estimate taken from [Laborde et al., 2019] is also reported in dark green. The blue dot indicates the shortening rate estimated on the Yecheng-Pishan anticline over the last ~5-7 Myr, from [5][Guilbaud et al., 2017]. The yellow star indicates the location of the Kekeya sedimentary section dated by magnetostratigraphy [Blayney et al., 2019; Zheng et al., 2015]. Satellite images are from https://www.bing.com/maps/. Dashed frame locates ***Figure 3****. a: anticline. D. Simplified geological section across the Western Kunlun Range and southwestern Tarim Basin showing the different morpho-structural ensembles that compose the mountain belt and its foreland basin (see location AA' on* ***Figure 1.C****). The subsurface data used to construct the section are from [X-D Jiang et al., 2013] and [Laborde et al., 2019]. KF: Karakax fault; TKT: Tam Karaul thrust; TT: Tiklik thrust; WKFR: Western Kunlun Frontal blind Ramp; MT: Mazar Tagh thrust.*

2.3. Stratigraphy

The general stratigraphic framework of the WKR and southwestern Tarim Basin is summarized in the lithostratigraphic chart of **Figure 2** [for further details, see *Laborde et al.*, 2019 and references therein].

2.3.1. Inner range

The inner range is composed of an Archean to Proterozoic basement corresponding to igneous and metamorphic rocks overlain by Proterozoic to lower Paleozoic meta-sediments **(Figure 2)**. The metamorphism that has affected this basement and its cover is related to an early Paleozoic orogenic event [e.g., *Matte et al.*, 1996]. According to outcrop observations and well data, this metamorphosed sedimentary cover is only found in the inner range and the proximal part of the foothills [e.g., *Laborde et al.*, 2019].

2.3.2. Foothills

In the foothills, the basement is similar to the one of the inner range. Here, however, it is overlain by a more or less continuous sedimentary series, extending from Neoproterozoic (Sinian) to Quaternary, interrupted by two major hiatuses **(Figure 2)**. The first hiatus forms an angular unconformity sealing a thin-skinned deformation related to the early Paleozoic orogenic event mentioned above [*Y-J Li et al.*, 2016a]. The second hiatus forms an angular unconformity that has eroded the previously deposited Mesozoic sediments, and that is related to a poorly understood long-wavelength deformation occurring at the end of the Cretaceous [*Y-J Li et al.*, 2016b].

From Sinian to Carboniferous, the sedimentation was mainly marine with an alternation of calcareous, terrigenous and gypsiferous deposits, among which the evaporitic interval of the middle to upper Cambrian detachment level. Continental transition occurred during the Permian, which is dominated by a terrigenous sedimentation. Successive marine transgressions re-invaded the area during Paleocene and Eocene, as recorded by calcareous deposits, as well as massive gypsum beds and reddish-brown gypsiferous mudstones corresponding to the detachment level at the base of the Cenozoic deposits. The last retreat

of the sea occurred during late Eocene and was followed by terrigenous sedimentation, which mostly consists of claystones, siltstones and sandstones (Figure 2).

The Miocene to Pliocene sedimentation corresponds to wedge-top deposits associated with the reactivation of the WKR thrust wedge. This reactivation results in a long-term upward coarsening sequence, with a progressive increase of gravel content **(Figure 2)**. A magnetostratigraphic section obtained along the Kekeya River **(Figure 1.C)** constrains the onset of this syn-tectonic sedimentation between ~22 Ma and ~15 Ma [*Blayney et al.*, 2019; *Zheng et al.*, 2015].

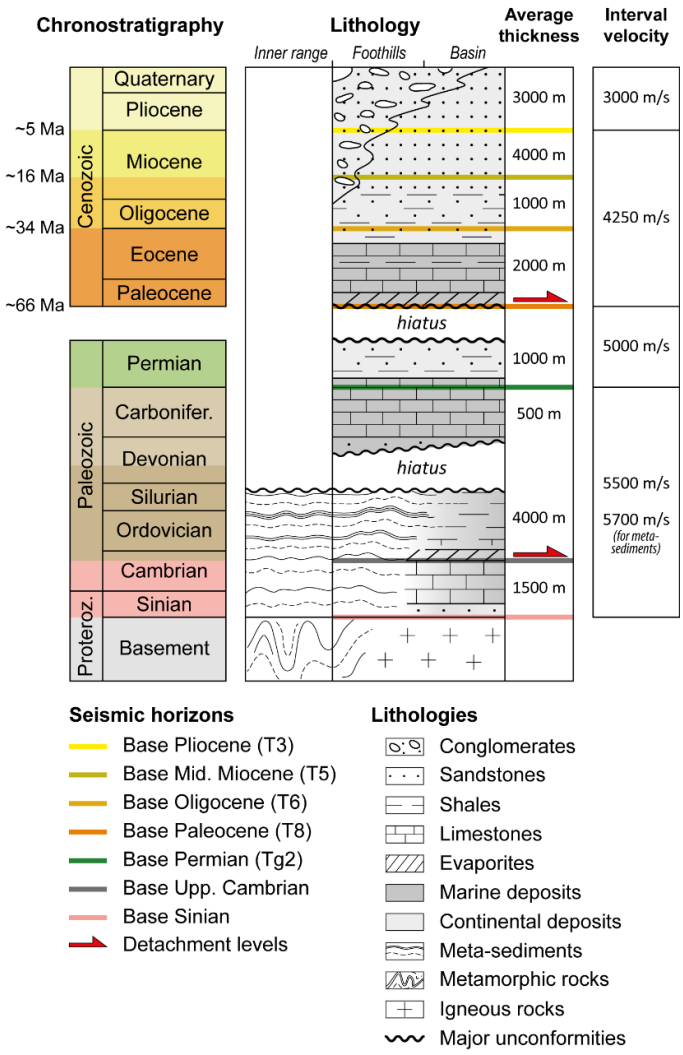

Figure 2: *Simplified chronostratigraphic chart of the Western Kunlun Range and its foreland basin, modified from [Laborde et al., 2019]. Key seismic horizons are reported, and interval velocities considered for depth-conversion of the seismic profiles are indicated.*

2.4. The Hotan anticline

The Hotan anticline is located to the west and southwest of the city of Hotan **(Figure 1)**. It forms a ~120 km-long and ~15-20 km-wide east-west-striking fold, with a maximum topographic expression of ~700-800 m above the present-day Tarim sedimentation base level **(Figure 3)**. Due to these large dimensions, this fold is a major structure of the Western Kunlun foothills.

The structural geometry proposed for the Hotan anticline is very different from other foothill anticlines further west (i.e. Yecheng-Pishan, Kekeya, Fusha, and Pusikai anticlines), which are interpreted as blind imbricated thrusts and duplexes [e.g., *H L Chen et al.*, 2018; *Guilbaud et al.*, 2017; *X-D Jiang et al.*, 2013; *Laborde et al.*, 2019; *Li et al.*, 2021; *T Li et al.*, 2016; *T Sun et al.*, 2019; *C-Y Wang et al.*, 2013; *C Wang et al.*, 2016; *S Wang et al.*, 2021] **(Figure 1.C)**. Published seismic profiles reveal that near the Karakax and Yurungkax rivers **(Figure 3.A)**, the Hotan anticline rather corresponds to a major fault-bend fold over a north-verging ramp (the Hotan thrust) climbing from the Cambrian detachment level upward to the Paleocene detachment level [*Cheng et al.*, 2017; *X-D Jiang and Li*, 2014; *X-D Jiang et al.*, 2013]. The measured amount of total shortening ranges between ~27 km [*Cheng et al.*, 2017] and ~37 km [*X-D Jiang et al.*, 2013]. The seismic stratigraphic analysis of the growth strata lying over the forelimb of the anticline indicates that folding initiated during the middle Miocene [*Cheng et al.*, 2017].

232 To the east, where several previous studies were conducted [*Cheng et al.*, 2017; *X-D Jiang*
233 *and Li*, 2014; *X-D Jiang et al.*, 2013], only the upper part of the folded Cenozoic deposits is
234 exposed above the sedimentation level. To the west, in contrast to the other foothill
235 structures, the Hotan anticline deforms and exhumes deeper series, with Paleozoic units
236 cropping out in its core **(Figure 3.B)**. Accordingly, the structure of this fold seems to present
237 strong lateral variations. However, published data remain limited so far to discuss the lateral
238 variations observed in the surface geology along the anticline. Yet, it is essential to constrain
239 these variations in order to better document the overall deformation and lateral changes in
240 the foothills of the Western Kunlun, in which this fold represents a major, though atypical
241 structure.

242 ## 3. Data and methods

243 ### *3.1. Data*

244 To build a geological map of the study area **(Figure 3.B)**, we combine satellites images
245 (Google Earth database) and existing cartographic documents [*Guilbaud et al.*, 2017; *C*
246 *Wang et al.*, 2016; *Y Yang et al.*, 2009 and unpublished geological maps from Tarim oil
247 companies], together with field observations along river sections crossing the Hotan
248 anticline **(Figure 4)**.

249 In addition to these surface constraints, the subsurface geometry of the anticline is
250 documented by forty-two 2D-reflection seismic profiles acquired in 1996, 1997, and 1998,
251 by the Sinopec Group of the China Petrochemical Corporation. Thirty lines are oriented
252 NNE-SSW, perpendicular to the structural trend, while twelve are oriented NW-SE, parallel

to the fold axis **(Figure 3.A)**. Subsurface calibration of seismic horizons was done from surface geology and from the Hecan-1 well (80°E, 36.9°E), which was drilled by the Shengli Oil Complex in 1997, through a 5404 m-thick sedimentary series formed by Quaternary, Neogene, Paleogene, Permian, Carboniferous, and Silurian-Devonian strata.

3.2. Methods

3.2.1. Seismic Interpretation

Observable seismic reflectors are followed to delineate the subsurface geometry of the Hotan anticline on seismic profiles. Offsets of these reflectors are used to identify faults. Seven key horizons are emphasized. These are the base of the: Sinian, Upper Cambrian, Permian (Tg2), Paleocene (T8), Oligocene (T6), middle Miocene (T5) and Pliocene (T3) series **(Figure 2)**. These horizons were previously identified at a regional scale and their age constrained by a compilation of biostratigraphic and magnetostratigraphic data from cores and surface outcrops [*Laborde et al.*, 2019]. To ensure a consistent and comparable interpretation of the various sections, the selected seismic horizons are propagated over the whole seismic grid, from one seismic profile to the other. We more specifically analyse eighteen seismic profiles to determine the structural geometry of the Hotan anticline and its variations along strike **(Figures 3.A, 5, and 6)**.

3.2.2. Depth conversion

Once interpreted, the two-way-time seismic profiles are depth-converted using constant velocity intervals based on velocity data derived from four wells within the Tarim Basin

[*Laborde et al.*, 2019]. Calibration of the velocity model is adjusted with data from the Hecan-1 well. The used velocity intervals are indicated in **Figure 2**.

3.2.3. Building balanced cross-sections

In order to characterize the structural geometry of the Hotan anticline, surface and seismic reflection data are integrated to construct four ~70 km-long balanced cross-sections, extending from the Tiklik thrust at the rear of the Hotan anticline, to the southwestern Tarim Basin **(Figures 3 and 7)**. These sections are balanced using the Move structural software, following an approach based on bed length and thickness conservation, and assuming folding by flexural-slip. The final cross-sections can be restored at the top of the Oligocene deposits (assumed to be horizontal at the time of deposition) and pinned at local pin lines in the foreland.

3.2.4. Growth strata analysis

The geometry of the growth strata and their variations along strike are then analysed on eighteen seismic profiles across the Hotan anticline **(Figures 3.A and 8)**. In addition to the regionally-correlated seismic horizons T5 (base of the middle Miocene) and T3 (base of the Pliocene), nine growth horizons (horizons labelled a, b, c, d, e, f, g, h, i) are defined on seismic profiles and correlated from one section to the other through the seismic grid, so as to compare the geometry and timing of growth strata along strike. Their age is estimated from the accumulation rates deduced from dated horizons T5 and T3, assuming constant accumulation rates during the corresponding time intervals. These age estimates are determined for each profile, within the foreland, i.e. north and out of the folded area.

4. Structural architecture and shortening

4.1. Surface geology

Figure 3.B illustrates our geological map of the Hotan anticline and surrounding area. To the south, the local WKR foothills are bounded by the Tiklik thrust. At the front of this thrust, two narrow thrust-related anticlines, parallel to the range, are observed in the western part of the study area. They give rise to a large syncline filled by Miocene to Quaternary growth strata that are poorly constrained by field and seismic observations.

To the north, the Hotan anticline is NW-SE-oriented and ~120 km long **(Figure 3.B)**. Deep stratigraphic levels, down to Silurian phyllites **(Figure 4.A)**, are exhumed in the northwestern part of the anticline, where the fold width reaches ~15 km. Laterally, the fold axis plunges eastward and gets gradually buried under Miocene to Quaternary syn-orogenic sediments. The anticline is asymmetrical, with dip angles of 15° to 30°S in the backlimb and dip angles of 20° to 90°N in the forelimb **(Figure 4.B)**. Dip angle values gradually decrease from west to east.

In the western part of the anticline, the backlimb is locally truncated by a north-verging thrust, which duplicates the Permian and Paleogene series **(Figure 3.B)**. The forelimb of the fold anticline is then bounded by an intra-Miocene erosional unconformity that truncates (i) the Permian to Paleogene (Paleocene-Eocene) strata to the west, and up to (ii) the Miocene strata towards the east **(Figure 3.B)**. Dip measurements across the forelimb show that this unconformity corresponds to an angular one between the north-dipping Paleogene strata

(70°-90°N) and the more recent growth strata further north, with dip angles that gradually decrease to almost horizontal (15°-4°N) **(Figure 4.B)**.

Finally, to the east of the study area, the Aqik tear fault is oriented approximately north-south and exhumes series down to the Silurian-Ordovician **(Figure 3.B)**.

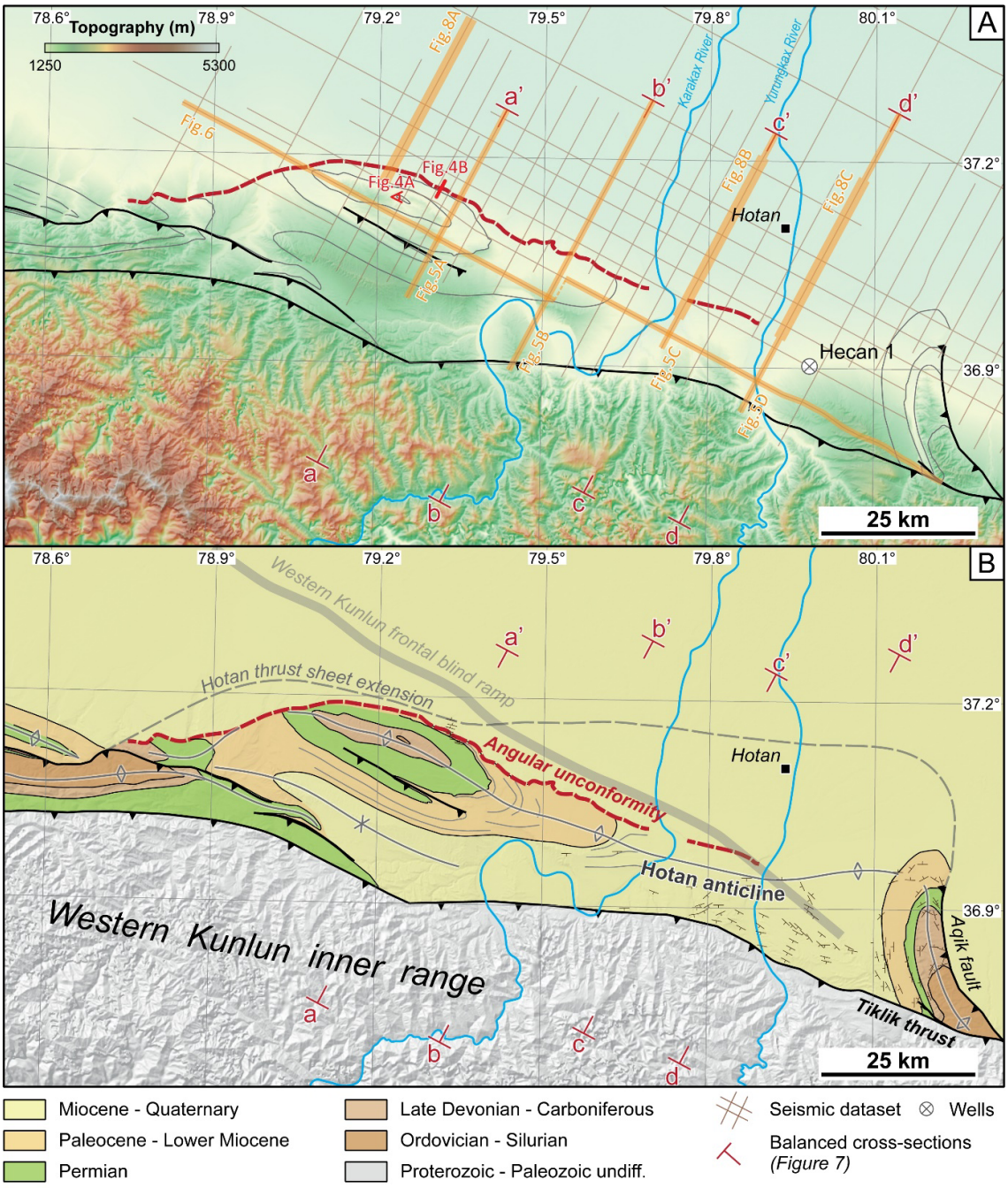

Figure 3: *Map of the study area (location on* ***Figures 1.B and 1.C****). A. Topographic map and seismic dataset used in this study. Elevation data are from NASA Shuttle Radar Topography Mission (3arc-second resolution) [Jarvis et al., 2008]. Thin orange lines locate the whole seismic grid used in this study. Sections of* ***Figures 5, 6 and 8*** *are reported by labelled large orange lines. Cross-sections of* ***Figure 7*** *(aa', bb', cc' and dd') are indicated. Field*

*observations of **Figure 4** are also located. B. Geological map, illustrating the extension of the Hotan thrust and the location of the most frontal ramp of the underlying blind duplex. Cross-sections aa' to dd' of **Figure 7** are reported.*

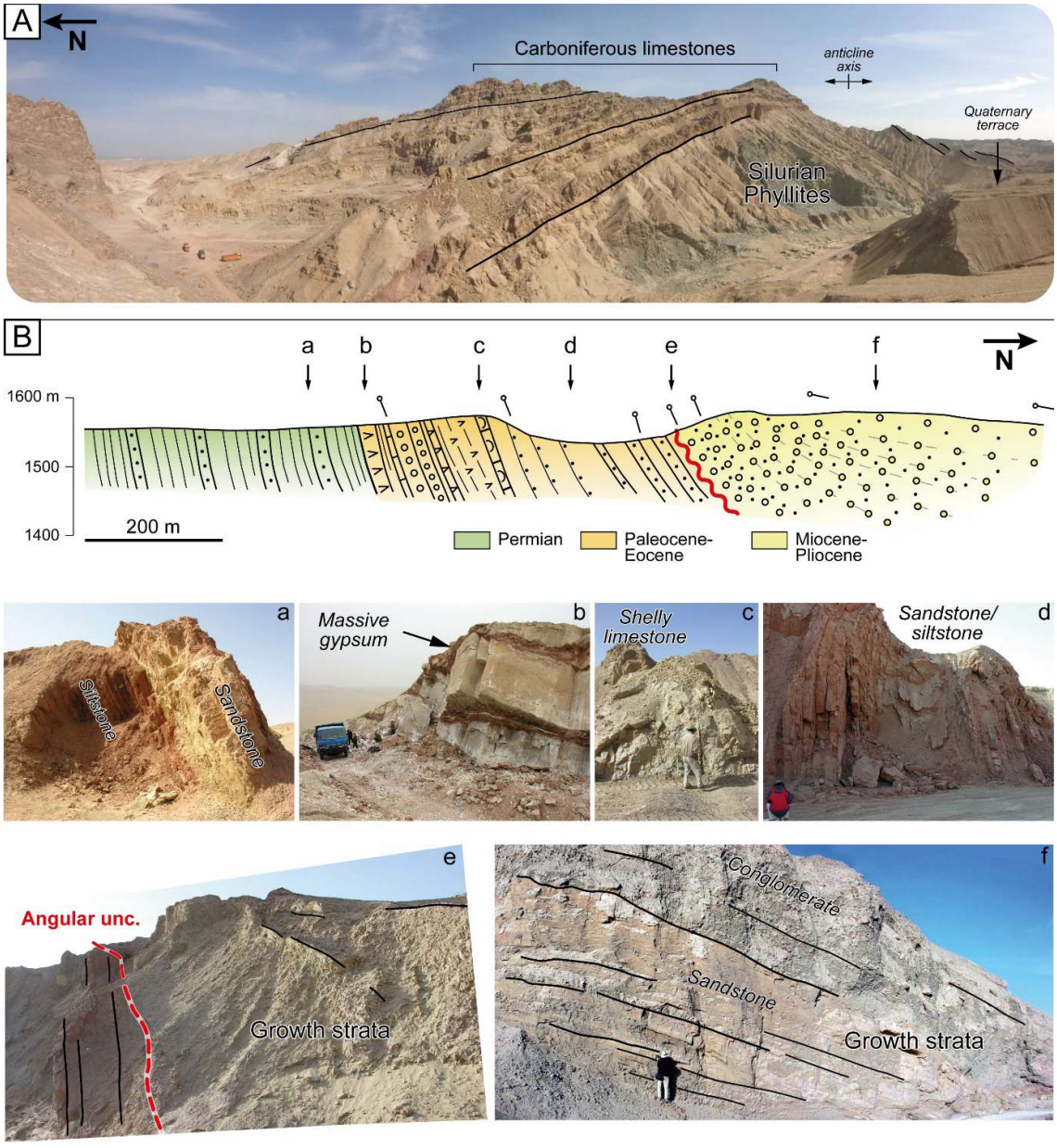

***Figure 4**: Field pictures and observations. A. Photo from the core of the Hotan anticline (see location on **Figure 3.A**). Note the meta-sediments that outcrop at the base of the Carboniferous limestones. Trucks in the lower left side for scale. B. Schematic surface cross-*

*section of the northern limb of the Hotan anticline (see location on **Figure 3.A**) and photos (a, b, c, d, e and f) of the corresponding sedimentary facies.*

4.2. Interpreted seismic profiles

The deep structure of the Hotan anticline is illustrated here by four NNE-SSW-oriented seismic profiles **(Figure 5)** and one WNW-SSE-oriented composite seismic profile **(Figure 6)**. These interpreted profiles show a large overthrust, referred to as the Hotan thrust. The hanging wall unit of this thrust forms a broad unfaulted ramp anticline deformed by a duplex that developed in the footwall unit. According to seismic imaging, the Hotan thrust propagated from the Cambrian lower detachment to the Paleocene upper one. The underlying duplex developed between the Cambrian detachment and a shallower one at the base of the Permian series **(Figures 5.B.C)**, before connecting upward into the Paleocene detachment **(Figure 5.C)**. The Hotan thrust and the underlying footwall duplex are referred to as the Hotan thrust system.

A seismic facies analysis of the different sedimentary units involved in the Hotan thrust system is out of the scope of this study. Nevertheless, the older geologic formation involved in the Hotan thrust sheet displays chaotic and transparent seismic facies that strongly contrasts with the layered facies involved in the footwall duplex **(Figures 5 and 6)**. Surface and well data indicate that this chaotic facies corresponds to metamorphic Paleozoic sediments (i.e. phyllites) **(Figure 4.A)** found in the inner portion of the WKR **(Figure 2)**. Velocity pull-up beneath the Hotan thrust system is related to the higher seismic velocities of these meta-sediments **(Figure 2)**.

352 The different profiles clearly show that the amplitude and wavelength of the Hotan anticline
353 is related to the amplitude and area of the footwall duplex. Indeed, the duplex has a
354 maximum amplitude to the northwest of the anticline, where the deeper and older series
355 are exposed **(Figures 3.B, 5.A, and 6)**. The amplitude gradually decreases towards the
356 southeast where the duplex structure disappears **(Figures 5.D and 6)**. This variation in the
357 duplex amplitude also explains the lateral variation in the dip angles documented within the
358 limbs of the Hotan anticline, which are steeper towards the northwest.

359 A wedge of Miocene to Pleistocene growth strata onlaps the forelimb of the Hotan anticline,
360 with a progressive thickening of the strata towards the foreland **(Figure 5)**. Below this
361 wedge, the forelimb of the anticline is partially eroded by an erosional unconformity that
362 merges at depth with the base of the growth strata and connects at the surface to the
363 mapped angular unconformity **(Figure 3)**. The detailed geometries of these growth strata
364 and their variations along strike are described later on. The data do not permit clear
365 observations within the backlimb of the anticline, in particular for growth strata **(Figure 5)**.

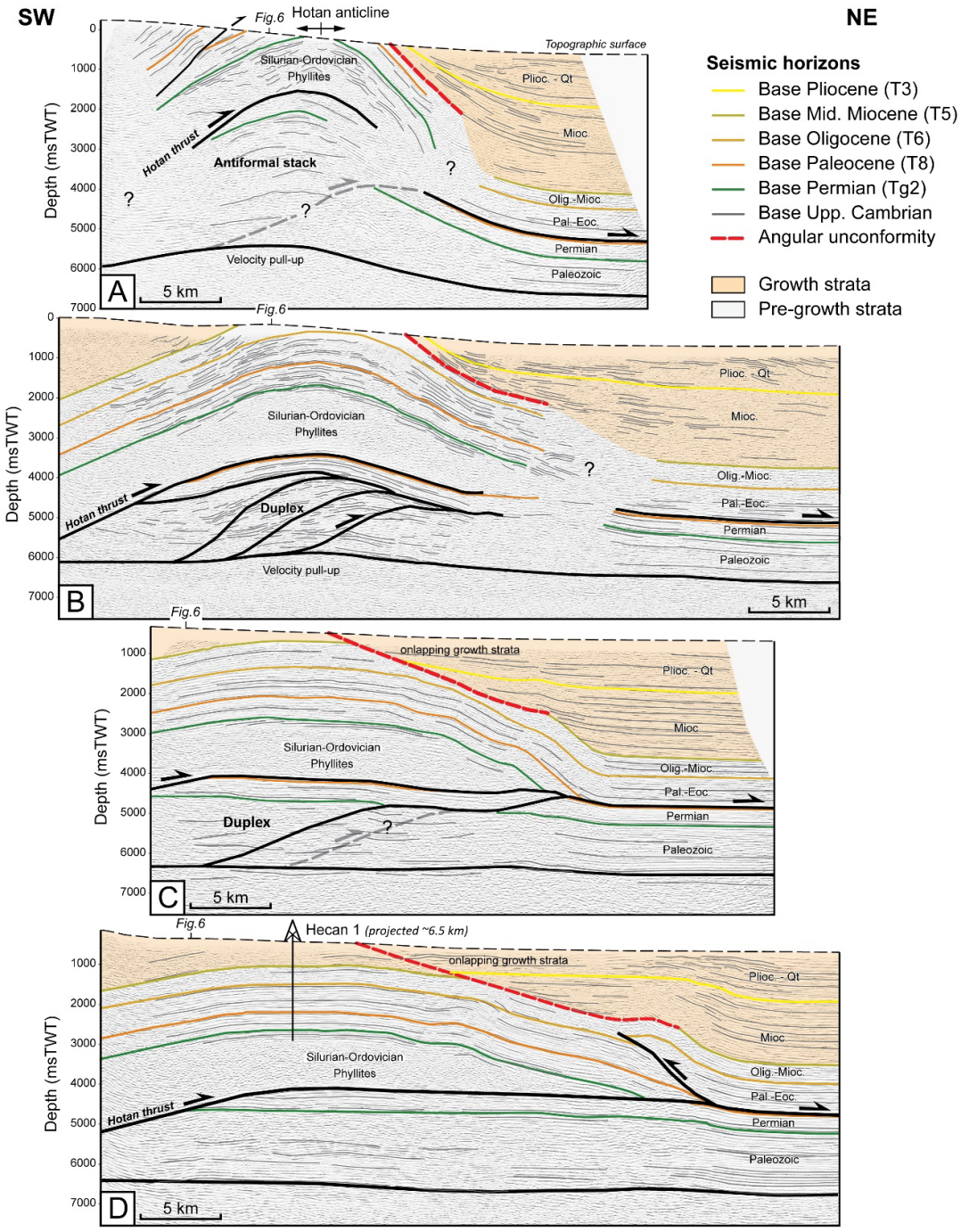

366

367 ***Figure 5****: Interpreted seismic reflection profiles across the Hotan thrust system illustrating its*

368 *structural variability along strike, from west (A) to east (D) (see location on* ***Figure 3.A****). Key*

369 *seismic horizons are color-coded and can be compared to the simplified regional*

370 *chronostratigraphic chart of* ***Figure 2****. Pre-growth and growth strata are differentiated.*

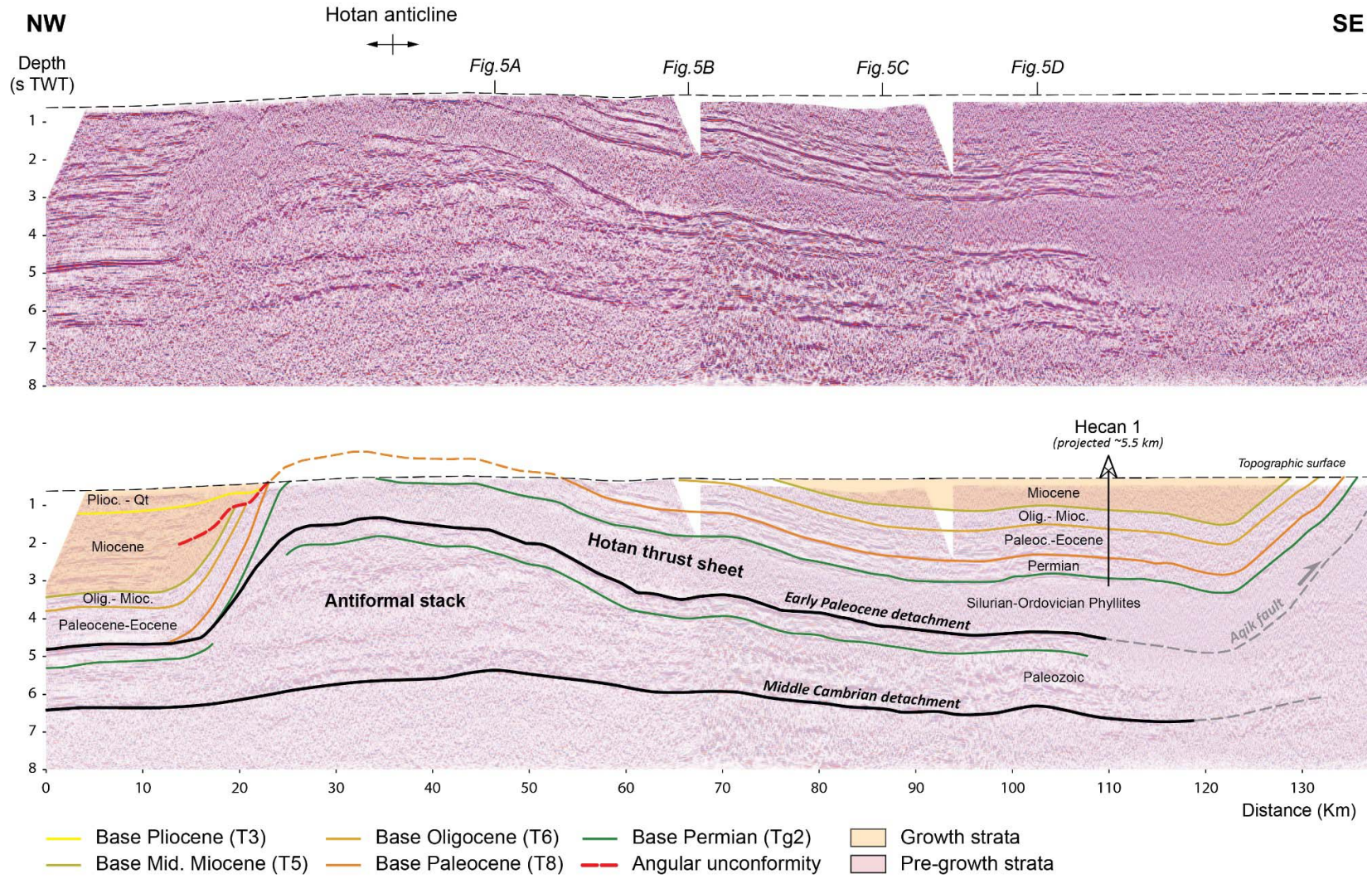
NW
SE
Hotan anticline
Depth
(s TWT)
Fig.5A
Fig.5B
Fig.5C
Fig.5D
Hecan 1
(projected ~5.5 km)
Topographic surface
Plioc. - Qt
Miocene
Olig.- Mioc.
Paleocene-Eocene
Antiformal stack
Hotan thrust sheet
Early Paleocene detachment
Middle Cambrian detachment
Aqik fault
Miocene
Olig.- Mioc.
Paleoc.-Eocene
Permian
Silurian-Ordovician Phyllites
Paleozoic
Distance (Km)
Base Pliocene (T3)
Base Mid. Miocene (T5)
Base Oligocene (T6)
Base Paleocene (T8)
Base Permian (Tg2)
Angular unconformity
Growth strata
Pre-growth strata

371

Figure 6: *Uninterpreted (top) and interpreted (bottom) composite seismic reflection profile oriented parallel to the axis of the Hotan anticline (see location on* ***Figure 3.A****). Note the progressive development of the footwall duplex toward the northwest, which deforms the Hotan thrust and brings the Paleozoic series to the surface. Seismic sections of* ***Figure 5*** *are located along the uninterpreted profile. Key seismic horizons are color-coded and can be compared to the simplified regional chronostratigraphic chart of* ***Figure 2****. Pre-growth and growth strata are differentiated.*

4.3. Balanced cross-sections and horizontal shortening

4.3.1. Cross-sections

Four balanced cross-sections are constructed from surface geology and seismic data across the Hotan thrust system and associated anticline, from the Tarim foreland to the Tiklik thrust **(Figure 7)**. We hereafter describe our findings for each one of them.

Section aa': The Hotan anticline consists first of a major ramp anticline caused by slip over the Hotan thrust, and subsequently folded by an underlying footwall duplex developed on thrusts connecting the Cambrian detachment level to the Paleocene one. To balance the section, a stack of three horses is proposed to fill the area between the roof thrust and the floor thrust. Behind the Hotan anticline, the southern end of the section is not imaged by the seismic profiles and poorly documented by field data. The presence of a syncline in surface geology between the Tiklik thrust and the Hotan anticline imposes a geometric gap in the footwall of the Tiklik thrust. To fill this gap and keep the cross-section balanced, we propose that the southern limb of the syncline is underlain by two horses between the two

393 regional detachments. These horses could be the lateral continuity of the outcropping
394 thrusts to the west located at the rear of the Hotan anticline **(section 4.1, Figure 3.B)**.
395 Altogether, a restoration at the top of the Oligocene series indicates that a total shortening
396 of about 64 km is accumulated along section aa'. The total shortening accommodated by the
397 sole Hotan thrust system is ~40 km, with 23.6 km (59% of the 40 km) absorbed by the Hotan
398 thrust and 16.4 km (41% of the 40 km) by the footwall duplex.

399 Section bb': the Hotan thrust appears to be also folded by an underlying duplex with three
400 main horses. However, these horses seem to develop on thrusts connecting the Cambrian
401 detachment level to the secondary one at the base of the Permian series. This geometry is
402 imposed by the undeformed continuous reflectors observable on the seismic profiles within
403 the Permian series comprised in between the top of the horses and the Hotan thrust **(Figure**
404 **5.B)**. Further north, just at the front of the Hotan anticline, a secondary ramp connects the
405 base of the Permian series to the main detachment located within the Paleocene series.
406 Here again, the southern extent of the section is poorly constrained and a secondary splay
407 of the Tiklik thrust is proposed to balance the section beneath the syncline documented in
408 surface geology. Altogether, the total shortening accumulated across the whole section is
409 ~47.5 km. The total shortening across the Hotan anticline is 34.5 km, with 28.5 km (82.6% of
410 the 34.5 km) accommodated by the Hotan thrust and 6 km (17.4% of 34.5 km) by the
411 footwall duplex.

412 Section cc': The structural architecture of the Hotan thrust system is similar to the one
413 along section bb', with a duplex displaying two horses beneath the Hotan thrust. Here, the
414 Tiklik thrust directly overthrusts the Hotan anticline and the absence of a syncline leads to
415 no additional blind thrust or duplex. The total shortening across the Hotan anticline is ~34.8

416 km with 33.5 km (96.3% of 34.8 km) consumed by the Hotan thrust and 1.3 km (3.7% of 34.8
417 km) by the footwall duplex.

418 Section dd': The Hotan thrust system consists of an isolated major ramp anticline, as in
419 previous sections, but with no underlying duplex. This ramp anticline absorbs about 35.5 km
420 of total shortening. The Paleogene series of the forelimb of the anticline are folded in a
421 secondary small-scale anticline related to a backthrust rooting into the Paleocene
422 detachment. This secondary thrust accommodates around 2 km (5.6%) of the total
423 shortening.

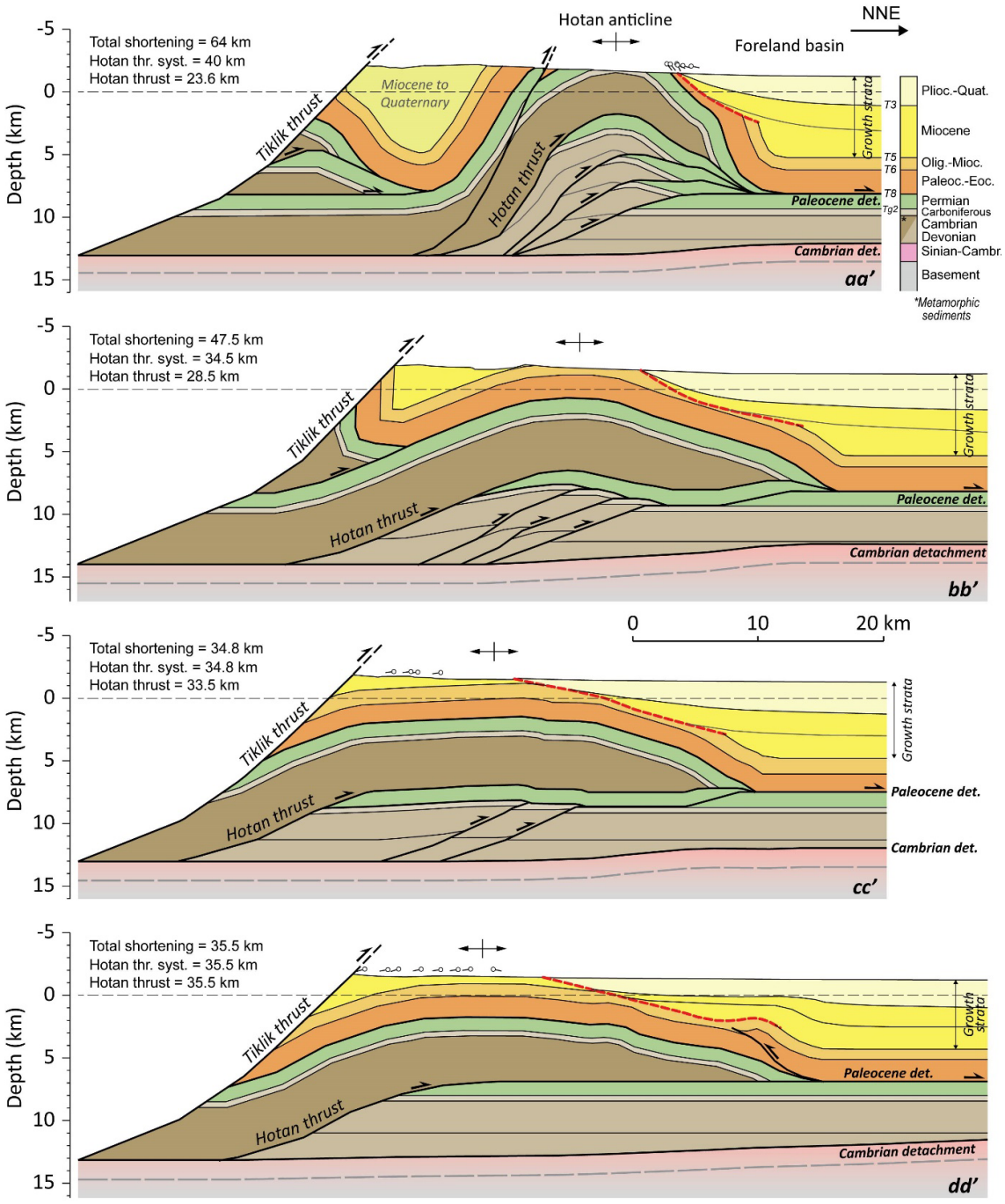

424

425 ***Figure 7:*** *Balanced cross-sections across the foothills of the Western Kunlun Range and*
426 *associated shortening values (see location on* ***Figure 3.A****). Growth strata are reported in the*
427 *forelimb of the Hotan anticline. Key horizons and layers are indicated, as well as their*
428 *stratigraphic age (section aa'). The restored sections are shown in* ***Figure S1****.*

4.3.2. Along-strike variations in shortening and structural style

Our observations show that the Hotan anticline results from a major blind thrust sheet involving Silurian-Ordovician meta-sediments. This thrust sheet is deformed and folded over a footwall blind duplex. This structural style is found all along the Hotan anticline, except for the easternmost sections where the duplex is absent **(Figure 7)**. The total amount of shortening absorbed by the Hotan thrust system is relatively constant along strike, with a minor eastward decrease from ~40 to ~35 km. However, our results emphasize the existence of strong lateral variations in the partitioning of shortening. Indeed, the comparison between sections aa' to dd' reveals that the amount of shortening accommodated by the Hotan thrust increases eastward from ~23.6 to ~35.5 km, while the one accommodated by the footwall duplex decreases from ~16.4 to 0 km **(Figure 9.A)**. The respective contribution of the Hotan thrust and of the footwall duplex to the total shortening across the Hotan thrust system is thus fairly of the same order of magnitude to the west (60% vs. 40%, respectively - **Figure 9.A, section aa')**, but it strongly varies along-strike, with an eastward increasing contribution of the Hotan thrust (up to 100% - **Figure 9.A, section dd'**). When combined with the along-strike variations observed in the surface geology **(Figure 3.B)**, this partitioning indicates that the surface expression and morphology of the Hotan anticline is rather the indirect reflection of the deformation cumulated on the underlying blind duplex than that of the overlying large ramp anticline.

Overall, we find strong lateral variations in the deformation accommodated in the local Western Kunlun foothills (i.e. north of the Tiklik thrust), with a total shortening of ~64 km **(Figure 7, section aa')** that significantly decreases eastward to ~35.5 km **(Figure 7, section dd')**. This decrease is related to the significant shortening also accommodated by the blind

structures inferred beneath the synclines in the backlimb of the Hotan anticline, which are needed to balance the westernmost sections. In contrast, these structures are absent in the easternmost sections **(Figure 7, sections cc' and dd')**.

5. Kinematics of shortening as inferred from growth strata

5.1. Growth strata geometries

The backlimb of the Hotan anticline is poorly imaged by seismic data. Therefore, we rely only on the growth strata observable in its forelimb, either on seismic profiles or outcropping in the western portion of the structure **(Figures 4.B.e.f)**. Among the eighteen seismic profiles used to investigate the deep geometry of the growth strata and its variations along strike, three of them are shown in **Figure 8** to illustrate and synthesize our observations. Most of these profiles partially overlap our cross-sections of **Figure 7** (see locations on **Figure 3.A**).

Overall, the growth strata form a wedge thinning southward. They consist of Miocene to Quaternary beds that onlap an angular unconformity visible on the seismic profiles, as well as at the surface in the field **(Figure 3 and picture e in Figure 4.B)**. This indicates that the forelimb of the Hotan anticline was partially eroded during its growth. Associated with the unconformity, two packages of growth strata with different patterns are identified: (1) concordant growth strata, parallel with each other and with no lateral variations in thickness other than those related to their onlap over the eroded forelimb, at the bottom, and (2) fanning growth strata with upward shallowing dip angles and southward thinning of the layers toward the anticline, at the top. We hereafter describe in detail the growth strata of

473 the three profiles shown in **Figure 8**, with emphasis on these two patterns of growth strata
474 and their geometric relationships.

475 Profile A: This profile faces the core of the Hotan anticline, where deep stratigraphic series
476 are exhumed at the surface **(Figure 3.A)**. To the south of the profile, surface and sub-surface
477 observations indicate that the angular erosional unconformity separates steeply-dipping
478 pre-growth strata from onlapping, gently-dipping, growth strata fanning toward the basin
479 **(Figure 8.A)**. The erosion represented by the unconformity is significant, with at least ~2500
480 m of missing sediments **(Figure 7, section aa')**. Toward the basin, this angular unconformity
481 divides into two branches. The deeper branch separates the concordant growth strata
482 (growth horizons T5 to b) from the fanning ones that progressively onlap the unconformity
483 upward (updip from horizon b). Above, the upper branch forms a composite unconformity
484 [sensu *Ford et al.*, 1997; *Riba*, 1976] that separates growth offlap from growth onlap **(Figure**
485 **8.A)**. Altogether, the older growth strata developed above horizon T5, with concordant
486 growth strata found from T5 to horizon b, overlain by fanning growth strata from horizon b
487 to the top of the sedimentary series.

488 Profile B: This profile partly overlaps the section of **Figure 5.C** and cross-section cc' of
489 **Figure 7 (Figure 3.A)**. Here, the Hotan anticline is buried under growth strata **(Figure 8.B)**.
490 To the south of the profile, the angular unconformity observed at the surface separates sub-
491 horizontal growth strata at the top of the anticline from the younger northward gently-
492 dipping growth strata of its forelimb. Accordingly, along this section, the unconformity is
493 interpreted as a time-transgressive angular unconformity [sensu *Suppe et al.*, 1992]. Toward
494 the basin, this unconformity persists and separates at depth folded and eroded pre-growth
495 strata from the growth wedge developed above horizon T5. In this wedge, the two patterns

of growth strata mentioned above are observed with a first package of concordant strata from horizons T5 to < T3, and a second package of fanning growth strata from < T3 to the top of the sedimentary series **(Figure 8.B)**.

Profile C: This profile partly overlaps the profile of **Figure 5.D** and the cross-section dd' of **Figure 7 (Figure 3.A)**. Here again, the Hotan anticline is buried under the growth strata associated with a time-transgressive unconformity, even though this unconformity is much more tenuous **(Figures 8.C and 3)**. To the front of the fold, the proximal part of the growth wedge is characterized by concordant growth strata progressively onlapping its forelimb. As observed everywhere else, this growth wedge develops above horizon T5. At the base of this wedge, growth horizons between T5 to e are concordant but folded by the backthrust interpreted at the front of the anticline on the easternmost seismic profiles **(Figures 8.C, 5.D, and 7)**. In contrast, just above these folded horizons (i.e. from horizon e to the top of the sedimentary series), growth strata form fanning growth layers with an internal angular unconformity **(Figure 8.C)**.

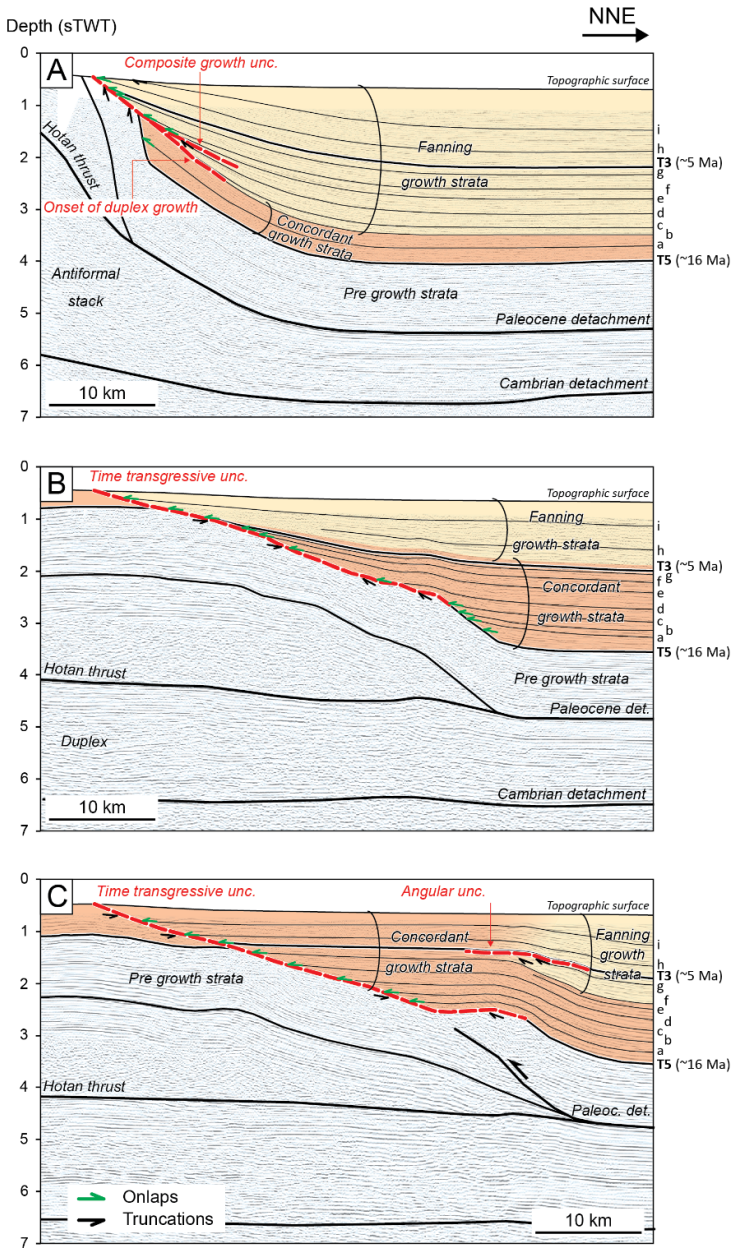

510

511 ***Figure 8****: Interpreted reflection seismic profiles showing the lateral evolution of the geometry*

512 *of the growth strata identified within the forelimb of the Hotan anticline (see location on*

513 ***Figure 3.A****). Note that the labelled seismic horizons on the right edge of the sections have*

514 *been correlated over the entire seismic dataset depicted in* ***Figure 3.A****. Two patterns of*

515 *growth strata are identified, with concordant and fanning growth strata.*

5.2. Folding mechanisms and timing of deformation

Growth strata geometries are primarily controlled by the folding mechanism (i.e. kink-band migration and limb rotation), as well as by the relative rates of sedimentation and uplift [e.g., *Shaw et al.*, 2005]. According to our seismic interpretations described above, two distinct patterns of growth strata are preserved in the forelimb of the Hotan anticline. The first deeper one corresponds to concordant growth strata onlapping pre-growth strata, which are observed all along the fold. Such a pattern is classically found at the forefront of fault-bend folds when the uplift rate exceeds the sedimentation rate [*Suppe et al.*, 1992]. We therefore propose to interpret these concordant growth strata as related to the deformation and forward propagation of the Hotan thrust **(Figure 10)**. To the top of the growth wedge, a second pattern corresponding to a fan of onlapping growth strata is observed in the sections where the duplex developed in the footwall of the Hotan thrust. This geometry is indicative of a mechanism of progressive limb rotation [e.g., *Hardy and Poblet*, 1994]. We thus rather interpret these fanning growth strata as related to the subsequent growth of the footwall duplex, with its stacking inducing local uplift, erosion, and overall progressive rotation of the overlying forelimb **(Figure 10)**. Finally, other fanning growth strata are also observed above the backthrust documented solely in the easternmost seismic profiles **(Figure 8.C).** These layers therefore seem to have recorded the late activation of this secondary structure to the east of the Hotan thrust system.

These two styles of growth strata can be identified throughout the seismic database used in this study. Based on this identification, we point out the seismic horizons affected by each of them to date the initiation of each folding style. To highlight the along-strike age variations

of the propagation of the Hotan thrust and footwall duplex, we synthesize our findings along the Hotan thrust system **(Figures 9 and 10)**. This synthesis shows that:

(1) growth strata develop everywhere upward from horizon T5, which implies a synchronous onset of deformation of the Hotan anticline dated to ~16 Ma at the scale of the whole study site.

(2) concordant growth strata are first deposited all along the forelimb of the Hotan anticline, consistent with an early activity of the Hotan thrust.

(3) a transition from concordant to fanning growth strata then occurs higher in the series, which points to a later activation of the footwall duplex below the fault-bend fold.

(4) this transition takes place at varying growth horizons all along the anticline, indicating that the growth of this duplex initiated diachronously over the study area. It occurs at the level of horizon b on the westernmost profiles and of progressively shallower horizons further east, revealing that the duplex growth initiated first to the west before gradually propagating eastward over time **(Figure 9.B)**.

(5) the fanning growth strata evidenced on the easternmost sections above the backthrust at the front of the Hotan anticline initiated by horizon f **(Figure 8.C)**, so that this local structure is interpreted to be a late feature initiating between ~16 and ~5 Ma.

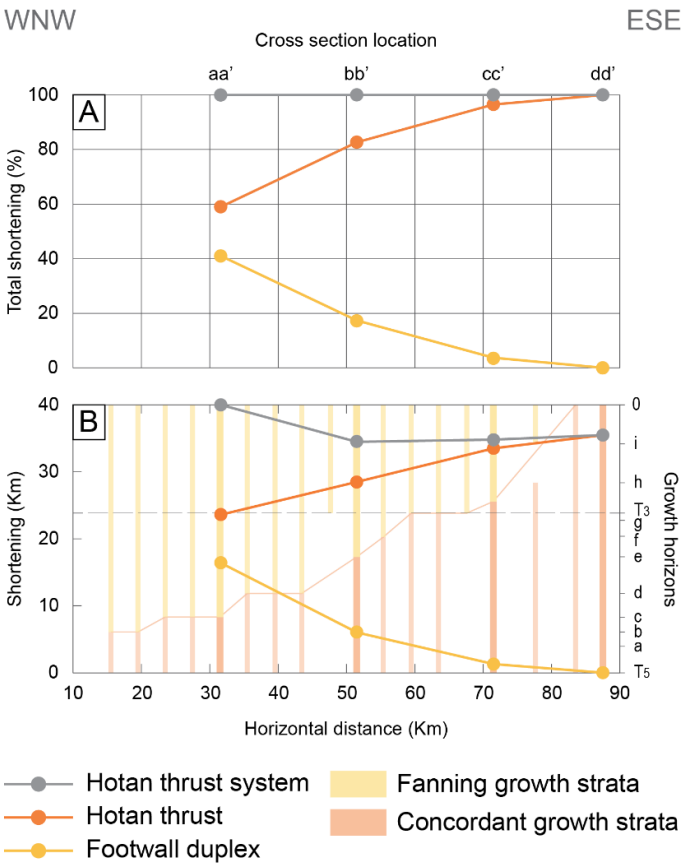

555

556 ***Figure 9****: Lateral variations in the shortening absorbed across the Hotan thrust system, and*
557 *in the age of the transition from the Hotan thrust to the footwall duplex. Total shortening is*
558 *reported for each section of* ***Figure 7****, and its partitioning between the Hotan thrust and the*
559 *underlying footwall duplex is indicated. A. Relative contribution of the Hotan thrust and of*
560 *the underlying duplex to total shortening for each section of* ***Figure 7****. B. Shortening and its*
561 *partitioning between the Hotan thrust and the underlying duplex for each section of* ***Figure***
562 ***7****. The patterns and the relative ages of the forelimb growth strata interpreted on the seismic*
563 *profiles that cross the Hotan anticline are projected for each section of* ***Figure 7****, and*
564 *additional sections of the available seismic grid* ***(Figure 3.A)****. Note that the concordant*
565 *growth strata pattern becomes dominant as the amount of shortening accommodated by*
566 *the footwall duplex gradually decreases eastward. Relative ages of growth horizons are*

reported relative to key identified seismic horizons T3 and T5 and labelled from a to i ***(Figure 8)****.*

5.3. Shortening rates over time

From published magnetostratigraphic constraints, ages of seismic horizons T3 and T5 were dated to ~16 Ma and ~5 Ma, respectively [see *Laborde et al.*, 2019 and references therein]. To get additional quantitative estimates on the ages of other growth horizons, we use layer thicknesses between horizons and assume constant sedimentation rates from T5 to T3, and from T3 to the top of the sedimentary series. We do this for each cross-section of **Figure 7**, considering the thicknesses between the horizons just at the front of the Hotan anticline.

By combining shortening estimates **(Figure 7)** with the timing of deformation deduced from the growth strata **(Figure 9.B)** and refined from the above estimated ages, we deduce average shortening rates for each section since the onset of deformation by ~16 Ma, as well as during the periods of activity of the Hotan thrust and of duplex growth **(Table 1)**. Our results first suggest a slight variation along strike in the average long-term shortening rate since ~16 Ma, with a rate of ~2.5 mm/yr along section aa', decreasing eastward to a rate of ~2.2 mm/yr along section dd'. Because the onset of deformation is everywhere dated to ~16 Ma, this variation is correlated with the slight lateral variation in total shortening **(Figures 7 and 9)**. Then, when considering each section, we find that the shortening rate across the Hotan thrust system has not been steady over time. Indeed, average shortening rates deduced over the earlier period related to the Hotan thrust activity are systematically significantly higher than those deduced during the subsequent time of duplex growth **(Table 1)**. The most recent average shortening rates across the Hotan thrust system are ~1.3 to

589 ~0.3 mm/yr, over a time period of ~12 Ma or ~4 Ma to present, from sections aa' to cc',
590 respectively.

591 In assessing average shortening rates over the earlier and later phases of folding, we take
592 advantage of the record of a clear change in folding style, from a single broad fault-bend
593 anticline to a duplex, as recorded in the growth strata, and use it as a temporal marker of
594 deformation. However, shortening rates during the two different folding phases are average
595 values, with no resolution in terms of potential variations within and during the considered
596 time intervals. Section dd', where the footwall duplex is absent **(Figure 7)**, clearly illustrates
597 this point. Along this section, we can only deduce an average shortening rate since ~16 Ma
598 with no resolution in a possible change of deformation velocity over time as found in the
599 other sections further west. Consequently, this implies that the structural change from the
600 Hotan thrust to the onset of the duplex may not be coeval with the slowing down of
601 deformation rates, which may alternatively occur during either one of the two folding
602 phases **(Figure 10)**.

603 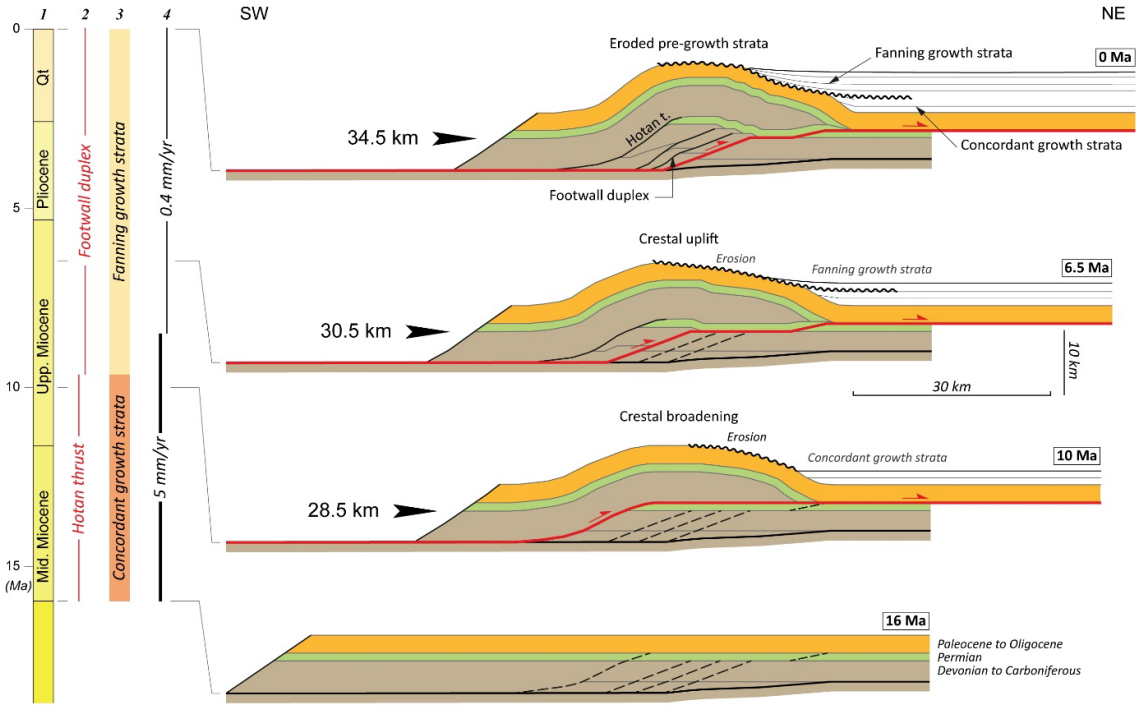

604 ***Figure 10:*** *Schematic sequential restoration of section bb' illustrating the kinematic and*
605 *structural evolution of the Hotan thrust system with associated growth strata geometry at*
606 *the frontal limb of the Hotan anticline. Note that the geometry of the growth strata at the*
607 *back of the anticline is not represented. Columns to the left indicate 1: Time; 2: Active*
608 *structures; 3: Growth strata geometry; 4: Shortening rates, as derived at the scale of the*
609 *whole Hotan thrust system (see* ***section 6.2.1*** *for further explanations). Note that the*
610 *deceleration in shortening rates by ~8-9 Ma is not coeval with the transition from the Hotan*
611 *thrust to the footwall duplex.*

612

	Sections	Hotan thrust system	Hotan thrust	Footwall duplex	Frontal backthrust
Shortening amounts	aa'	40.0	23.6	16.4	

(km)	bb'	34.5	28.5	6	
	cc'	34.8	33.5	1.3	
	dd'	35.5	35.5		2
Growth horizons	aa'	T5 - 0	T5 - c	c - 0	
	bb'	T5 - 0	T5 - e	e - 0	
	cc'	T5 - 0	T5 - < T3	< T3 - 0	
	dd'	T5 - 0	T5 - 0		f - 0
Durations (Myr)	aa'	16.0	3.8	12.19	
	bb'	16.0	6.4	9.64	
	cc'	16.0	12.2	3.80	
	dd'	16.0	16.0		8.3
Shortening rates (mm/yr)	aa'	2.5	6.2	1.3	
	bb'	2.2	4.5	0.6	
	cc'	2.2	2.8	0.3	
	dd'	2.2	2.2		0.2

Table 1: Shortening, timing of deformation and shortening rates estimated for the different structures that compose the Hotan thrust system and on each section of **Figure 7**. The duration was estimated from the analysis of the growth strata assuming that the propagation of the Hotan thrust is recorded by the concordant pattern, and the growth of the footwall duplex by the fanning pattern **(Figures 8, 9 and 10)**. Refer to the text for details on the approach.

6. Discussion

6.1. Structure and shortening across the Hotan thrust system, in the context of the Western Kunlun Range

6.1.1. Structure of the Hotan thrust system

We show in this study that the Hotan anticline structure is far from being cylindrical. Indeed, to the west, the Hotan thrust is folded by a footwall duplex, whose amplitude and shortening decrease eastward. The total amount of shortening, although relatively similar along strike, is partitioned between the Hotan fault-bend fold and the underlying duplex.

Previous studies only focused on the eastern part of the Hotan anticline and interpreted this structure as a north verging fault-bend fold [*Cheng et al.*, 2017; *X-D Jiang et al.*, 2013] **(see Section 2.4.)**. Indeed, as the underlying duplex is poorly expressed near the Karakax and Yurunkax rivers, it was not clearly identified in these previous structural interpretations **(Figure 3)**. However, *X-D Jiang et al.* [2013] noticed two secondary faults breaking the lower Paleozoic series below the Hotan thrust, which we re-interpret as two thrust horses in section cc' **(Figure 7)**. Along this cross-section, we also derive a total Cenozoic shortening of ~34.8 km, overall consistent with the values of ~37.5 km and ~27 km estimated by *X-D Jiang et al.* [2013] and *Cheng et al.* [2017], respectively. From our analysis of the growth strata, the deformation of the Hotan thrust system is interpreted to initiate by ~16 Ma, a timing which is also consistent with the Lower Miocene ages (23-15 Ma) proposed in these previous studies. Altogether, our results are therefore in line with previous interpretations in terms of structure, shortening and timing of deformation along the eastern Hotan

anticline. They complement these earlier views by documenting lateral variations in the structural architecture of the anticline, and by pointing out temporal changes in the kinematics of shortening further discussed hereafter (Section 6.2).

We only have limited evidence to discuss the causes of these lateral and temporal changes in kinematics along strike. Our balanced cross-sections show that the Hotan thrust developed along a stratigraphic and lithological contrast between the meta-sediments inherited from the Palaeozoic orogeny and the corresponding non-metamorphic sediments preserved in the Tarim Basin **(Figures 2, 7 and S1)**, pointing out the potential role of structural/lithological inheritance in the location of this structure, as noted in other studies [e.g., *Laborde et al.*, 2019]. The reason why shortening has been subsequently taken up progressively from west to east by a footwall duplex is not clear. One possibility could be related to the spatial extent and orientation of inherited structures, less favourable at some point than the neo-formed thrusts within the Tarim sedimentary sequence with regards to the direction of the Cenozoic regional compression. This idea is possibly supported by the fact that all structures of the inner range of the WKR, as well as the extent of the Hotan thrust, are oblique to the neo-formed structures of the foothills (i.e. Yecheng-Pishan and Kekeya anticlines) and of the Tarim Basin (Mazar Tagh thrust) **(Figure 1.C)**.

6.1.2. Contribution of the foothills to crustal shortening across the Western Kunlun Range

At the scale of the foothills (i.e. considering all the structures located north of the Tiklik fault), our cross-sections show that the total amount of shortening in the studied area increases laterally from ~35 km to the east (section dd') to ~64 km to the west (section aa').

This significant lateral increase over a distance of ~55 km is related to the westward growing contribution of thrusts suspected in between the Tiklik fault and the Hotan anticline (section aa'). Following the same crustal budget approach as *Laborde et al.* [2019], we assess a total shortening of ~70-60 km across the whole WKR at the longitude of section aa' (see **Figure S2**). According to this estimate, most of the crustal shortening (i.e. from ~50 % to 100 %) could be accommodated in the foothills of the range.

This proportion is considerably higher than that suggested by the cross-sections published further west, where only ~40 % of the shortening (~35 to ~28 km out of a total of 78±23 km) was proposed to be accommodated north of the Tiklik fault [*Laborde et al.*, 2019; *T Sun et al.*, 2019] **(Figure 1.C)**. However, in these earlier studies, the inner structures of the foothills are interpreted as basement thrust sheets rather than as duplexes involving the sedimentary series of the Tarim Basin. Yet, the seismic sections available across the Pusikai anticline clearly show that the inner part of the foothills corresponds to an antiformal stack with several horses of deformed Paleozoic and Mesozoic deposits above the Cambrian detachment level, which implies a significant amount of shortening of ~54 km **(Figure 1.C)** [*X-D Jiang et al.*, 2013]. The deformation style of such an antiformal stack is similar to the one of the Hotan footwall duplex, or to that located just at the front of the Tiklik thrust (section aa'). If such a deformation style is characteristic of the whole foothills, it is possible that certain structures initially interpreted as basement thrust sheets are in fact duplexes. If this were the case, the total amount of shortening accommodated across the outer WKR west of our study area could be significantly underestimated. In order to clarify this, a set of structurally self-consistent cross-sections is still needed for a rigorous comparison and discussion of the lateral variations in structure and shortening at the scale of the whole

685 foothills, and from there of the contribution of the foothills to the total crustal shortening
686 across the WKR.

687 *6.1.3. Up-dip transfer of thrust slip*

688 Previous interpretations [e.g., *Guilbaud et al.*, 2017; *Laborde et al.*, 2019; *T Li et al.*, 2016; *Lu*
689 *et al.*, 2016], as well as our cross-sections **(Figure 7)**, require transferring tens of kilometres
690 of slip up-dip onto the detachment level lying at the base of the Paleocene series. Here, two
691 scenarios are possible: the up-dip slip is transferred and consumed either (1) toward the
692 south, on a backward passive roof-thrust, or (2) toward the north into the Tarim Basin,
693 along a bedding-plane detachment at the base of the Paleocene series.

694 If slip had returned backward, the onlapping frontal growth strata would have been
695 overthrusted above the growing fold. In that case, their onlap terminations would be offset
696 and not observed anymore in place over the fold forelimb, with growth strata appearing
697 parallel to the underlying folded pre-growth layers [e.g., *Medwedeff*, 1989]. Accordingly, the
698 geometry of the growth strata identified within the forelimb of the anticline is not
699 compatible with backward passive roof-thrusting over the last ~16 Myr. Additionally, there
700 is no evidence for an emerging backward passive roof-thrust **(Figure 3)**. We acknowledge,
701 however, that the deeper part of the forelimb of the Hotan anticline is poorly imaged in
702 seismic profiles **(Figure 5)**, and that the geometrical record for a passive roof-thrust and
703 associated growth layers could be hidden in this area and/or lost by erosion along the
704 mapped erosional unconformity. The possibility of a backward up-dip slip transfer occurring
705 prior to the deposition of the onlapping growth layers can thus not be completely ruled out,
706 which would suggest an age of deformation initiation older than ~16 Ma. In any case, such a

backward passive thrust is presently kinematically not viable since the Paleocene detachment is disrupted by other faults (Tiklik fault or others) at the rear of the Hotan anticline **(Figures 3, 7 and 11)**. Backward thrusting early in the fold history would thus imply that these faults were emplaced out-of-sequence relative to the Hotan anticline thrust system, a scenario that does not seem to be in line with the thermochronological constraints published so far [*Cheng et al.*, 2017].

Altogether, the up-dip slip must have been transferred northward toward the foreland, at least over the last ~16 Myr. To the north, the foreland basin consists of sediments undeformed over a distance of ~175 km from the mountain front of the WKR, up to the Mazar Tagh thrust that reaches the surface **(Figures 1.C and 11)** [e.g., *Laborde et al.*, 2019]. This thrust roots into the Paleocene detachment and has a vergence synthetic to the structures of the WKR **(Figures 1.C and 1.D)**. We therefore favour the idea that the shortening absorbed across the Hotan thrust system and associated up-dip slip have been transferred northward onto the Paleocene detachment and into the Tarim Basin up to the Mazar Tagh thrust **(Figure 11)**, a kinematics in agreement with previous interpretations proposed from other structures of the foothills to the west of our study area [e.g., *Guilbaud et al.*, 2017; *Laborde et al.*, 2019; *T Li et al.*, 2016; *Lu et al.*, 2016], and in line with recent observations of migrating growth-strata with the Tarim foreland [*H Chen et al.*, 2022].

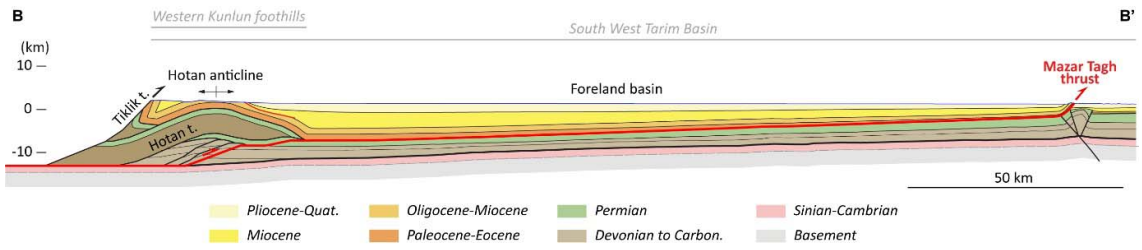

Figure 11: *Regional cross-section showing the Hotan anticline in its regional context. It illustrates how the shortening accommodated across the Hotan thrust system is transferred northward onto the Paleocene detachment at the base of the foreland basin and up to the Mazar Tagh frontal thrust. The subsurface data used to construct the section are from this study (section bb', Figure 7); [H J Yang et al., 2007] and [Laborde et al., 2019]. See location of BB' in* ***Figure 1.C.***

6.2. Temporal variations in the kinematics of shortening across the Hotan thrust system and their regional implications

6.2.1. An attempt at refining the deceleration of shortening rates across the Hotan thrust system

We show that the two structural units composing the Hotan thrust system have left a characteristic imprint in the growth strata. This imprint provides constraints on the timing of deformation by pointing the onset of duplex growth after the initial phase of fault-bend folding related to the Hotan thrust. Such a transition in the deformation style is used along each investigated cross-section to quantify shortening rates and reveal a significant deformation deceleration over time **(Section 5.3.)**.

The total amount of shortening across the Hotan thrust system is relatively homogeneous over the study area. Similarly, we do not find any evidence for lateral variations in the age of initiation of folding (~16 Ma, eventually earlier). Despite the obvious lateral variations in the partitioning of total shortening **(Figure 9)**, we hypothesize that the shortening rate and its temporal evolution could have been relatively homogeneous along strike. If this is correct,

747 the laterally non-coeval transition from fault-bend folding (related to the Hotan thrust) to
748 duplexing, derived in each section from growth strata, can be used as a passive marker of
749 the deformation to further refine the temporal evolution of the shortening rate at the scale
750 of the whole structure. To test this idea, we compare the timing of the tracked kinematic
751 change with the cumulated shortening at the time of this transition on each section **(Figure**
752 **12)**. The age of the onset of the backward thrust at the front of the Hotan anticline on
753 section dd' can also be taken into account. Considering that the entire shortening of ~35-40
754 km has been absorbed since ~16 Ma, this comparison illustrates and refines the possible
755 temporal variations in the shortening rate that were already suspected on each balanced
756 cross-section **(Table 1)**. These results confirm a first period of rapid deformation with a rate
757 of ~5 mm/yr, followed by a sharp deceleration by ~8-9 Ma with a subsequent average
758 shortening rate of ~0.4 mm/yr **(Figure 12)**.

759 We recall that this result only holds if shortening rates can be considered as homogeneous
760 along strike at the scale of the whole Hotan thrust system. In addition, the earlier high
761 shortening rate derived here may be over-estimated in the case that deformation started
762 earlier than 16 Ma. However, although this finding should be taken with extreme caution, it
763 questions the kinematic evolution of deformation along the foothills of the WKR and calls
764 for the search of additional evidence of this kinematic change.

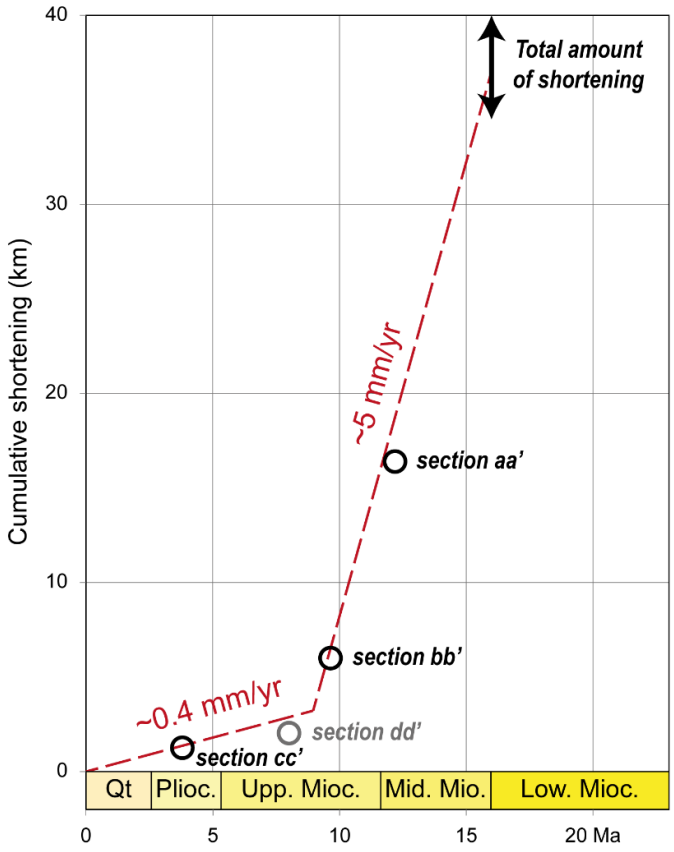

765

766 ***Figure 12:*** *Cumulative shortening on the Hotan thrust system, when restoring deformation*
767 *back in time. Deformation is considered to have initiated at ~16 Ma, with a total amount of*
768 *shortening of 35-40 km (double black arrow at the top right)* ***(Table 1)****. The clearly recorded*
769 *transition from the Hotan thrust to the onset of the footwall duplex on sections aa', bb' and*
770 *cc' is used as a marker of ongoing deformation (black circles). As such, the timing of this*
771 *transition, as well as the shortening cumulated backward in time from present-day to the*
772 *moment of this transition (i.e. across the sole footwall duplex), are reported for these*
773 *sections* ***(Table 1)****. In the case of section dd', the shortening cumulated on the late*
774 *backthrust at the front of the Hotan ramp anticline is reported with the onset time of this*
775 *structure (grey circle). In the case that shortening rates are homogeneous along strike at any*
776 *time, despite the variability of structural styles, these data taken together illustrate a clear*

deceleration of shortening rates (dashed red lines) by ~8-9 Ma at the scale of the whole Hotan thrust system.

6.2.2. Exploring possible kinematic changes at the scale of the Western Kunlun Range

We explore here whether or not the kinematic evolution suspected for the Hotan thrust system could be representative of the entire WKR. In the case of the Yecheng-Pishan anticline located ~130 km further west along strike **(Figure 1.C)**, *Guilbaud et al.* [2017] estimated a shortening rate of 2 to 2.5 mm/yr over the last 5.5 to 7 Myr from structural restoration and analysis of growth strata. At approximately the same longitude as the study of *Guilbaud et al.* [2017], an average long-term shortening rate of ~1.5 mm/yr over the last 25 Myr can be derived from the incremental restoration of *T Sun et al.* [2019]. Taken together, these rates seem inconsistent with our deductions for the Hotan thrust system since they rather depict an increase of deformation rates further west since the late Miocene. However, as discussed above **(Section 6.1.2.)**, the total shortening values estimated on other published sections cannot be directly compared to our results and may even not be inter-comparable as they do not derive from a self-consistent structural analysis of the various structures.

As stated previously, the proposed structural interpretations of the inner part of the foothills are debatable. Actually, the total shortening proposed by *T Sun et al.* [2019] is probably underestimated as their interpretation relies on the existence of basement thrust sheets in the inner foothills. In contrast, the most frontal thrusts of the foothills are undoubtedly connected to a Cambrian detachment level similar to that of the Hotan

799 structure [e.g., *Guilbaud et al.*, 2017; *Li et al.*, 2021; *T Li et al.*, 2016; *T Sun et al.*, 2019]. We
800 thus consider that the interpretation by *Guilbaud et al.* [2017] of the Pishan anticline in the
801 outer foothills can be compared to our results, but not to those of [*T Sun et al.*, 2019].
802 Therefore, the shortening acceleration suggested by the comparison of these two studies is
803 far to be demonstrated. Additional investigations of the total shortening across the
804 Yecheng-Pishan anticline and the structures at its rear are therefore needed.

805 Since the Late Miocene, the shortening rate across the Pishan anticline [*Guilbaud et al.*,
806 2017] appears significantly higher than that estimated across the Hotan anticline over the
807 same time interval (this study). This significant difference is most probably related to a
808 westward increase in the amount of total shortening accommodated across the foothills of
809 the WKR. This would be in line with the findings at the scale of our investigated area where
810 the shortening absorbed north of the Tiklik thrust increases from ~35 km to ~64 km
811 westward **(Figure 7)**. This is also suspected at a much larger scale when compared to some
812 of the cross-sections published west of our study area [e.g., *X-D Jiang et al.*, 2013; *S Wang et*
813 *al.*, 2021].

814 In our current state of knowledge, it is difficult to conclude whether the temporal variations
815 in deformation rate highlighted for the Hotan thrust system could also have occurred
816 laterally on other folds of the foothills. Nevertheless, on a larger scale, the sections available
817 in the Tarim Basin show a contemporaneous slowing down of the thick-skinned deformation
818 of the Bachu uplift during the Neogene [e.g., *Z Jiang et al.*, 2018; *Laborde et al.*, 2019; *Y-J Li*
819 *et al.*, 2016b; *Song et al.*, 2021; *Tong et al.*, 2012], a structure which also belongs to the
820 Western Kunlun thrust wedge [*Laborde et al.*, 2019; *Song et al.*, 2021]. This may point to a

821 regional deceleration of the deformation rates across the WKR and related structures, in
822 agreement with our deductions at the scale of the sole Hotan anticline.

823 *6.2.3. Regional implications*

824 In the case that the assumed late Miocene slowing down of shortening is real and that it
825 occurred at the scale of the foothills of the WKR, it can reflect either (1) a deformation
826 transfer towards the inner range, or (2) a general deformation deceleration across the
827 entire mountain range. However, the fact that the shortening could be almost entirely
828 accommodated across the foothills of the range **(Section 6.1.2 and Figure S2)** does not
829 plead in favour of the first hypothesis. Since the far-field convergence rate between Asia
830 and India and the shortening rate across the Himalayas do not seem to decrease over the
831 last ~10 Myr [e.g., *Lyon-Caen and Molnar*, 1984; *Molnar and Stock*, 2009; *Patriat and*
832 *Achache*, 1984], the shortening deceleration suspected at the scale of the WKR could rather
833 indicate a regional reorganization of the deformation in Central Asia. For example, it could
834 be the sign of a regional forward propagation of continental deformation to the north of the
835 Tarim Basin. Several studies on the southern Tian Shan support this hypothesis by
836 evidencing a contemporaneous acceleration of deformation across its foothills [e.g., *C Li et*
837 *al.*, 2019; *T Zhang et al.*, 2014], together with an acceleration of denudation in the inner
838 range [e.g., *Chang et al.*, 2021], since the late Miocene. A much more exhaustive study at a
839 broad regional scale would be nevertheless necessary to confirm this idea.

840 **7. Conclusion**

Surface geology and seismic imaging at depth reveal that the Hotan anticline is a non-cylindrical structure, formed by a broad ramp anticline, subsequently deformed by an underlying duplex. Cross-section balancing shows that the total shortening across the fold is partitioned between these two structural units, with a value slightly increasing westward from 35 to 40 km. The geometries of the growth strata found along the forelimb of the anticline show that deformation of this thrust system initiated during the middle Miocene (~16 Ma) at an average shortening rate of about 5 mm/yr, followed by a sharp deceleration with an average rate of about 0.4 mm/yr since ~8-9 Ma. Deceleration of the shortening rate happened independently of the transition from fault-bend folding to duplex stacking.

The Hotan anticline constitutes only part of the foothills of the WKR in the study area. Other blind thrust sheets are suspected at the rear of this fold to balance our cross-sections. Shortening across the foothills increases westward at the scale of the area investigated here, from ~35 km (absorbed solely by the Hotan thrust system) to ~64 km (taken up by the Hotan thrust system and other structures). At a more regional scale, we suggest that the foothills of the WKR accommodated most of the total crustal shortening of the range, most probably in a non-cylindrical way with shortening values increasing westward. A structural re-evaluation at the scale of the foothills is needed to accurately quantify and discuss these lateral variations in shortening along the front of the range.

Although this should be considered with caution, the deceleration of shortening rates identified in the case of the Hotan anticline could reflect a slowing down of the deformation at the scale of the whole WKR, possibly related to a regional reorganisation in link with a regional forward propagation of deformation into the Eurasian continent, north of the Tibetan Plateau.

Acknowledgments

This study is part of the 2nd Tibetan Plateau Scientific Expedition of the Ministry of Science and Technology of China (2019QZKK0901). This study also initiated thanks to a financial support from the INSU-CNRS ALEAS (PI: MS) and SYSTER (PI: LB) programs, from the Institut de physique du globe de Paris (IPGP - PI: MS), and from a travel support from the Program Hubert Curien Xu Guangqi (PI: MS and LH). It has subsequently been funded by the Agence Nationale de la Recherche through grant ANR-18-CE31-0008 (PI: MS). The seismic data used for this study are a courtesy of the Sinopec Group of the China Petrochemical Corporation. Petroleum Experts (Petex) is acknowledged for providing an academic licence of the Move software for structural modeling. This study contributes to the IdEx Université de Paris ANR-18-IDEX-0001. This is IPGP contribution # XX.

Data availability statement:

The Sinopec Group of the China Petrochemical Corporation provided the seismic reflection profiles used to constrain the geometry of the Hotan Anticline, as well as access to the data from the Hecan-1 well drilled in 1997. Five of these profiles are presented in this paper (Figures 5 and 6), the other data used in this study are a courtesy of the oil company and cannot be shared. The additional seismic reflection profiles used to build the two regional sections of this study (Figure 1.D and 11) are available through published work by Yang et al (2007), Jiang et al. (2013) and Laborde et al. (2019). The satellite data used for Figures 1 and 3 are from *NASA Shuttle Radar Topography Mission (3arc-second resolution) [Jarvis et al., 2008] and from https://www.bing.com/maps/.* Satellite images from the Google Earth database were also used in this work, together with published (Guilbaud et al, 2017; Wang

886 et al, 2016; Yang et al, 2009) and unpublished (property of Tarim oil companies) geological

887 maps.

References

Allègre, C. J., et al. (1984), Structure and evolution of the Himalaya–Tibet orogenic belt, *Nature*, *307*(5946), 17-22.

Avouac, J.-P., and G. Peltzer (1993), Active tectonics in southern Xinjiang, China: Analysis of terrace riser and normal fault scarp degradation along the Hotan-Qira Fault System, *Journal of Geophysical Research: Solid Earth*, *98*(B12), 21773-21807.

Blayney, T., G. Dupont-Nivet, Y. Najman, J. N. Proust, N. Meijer, P. Roperch, E. R. Sobel, I. Millar, and Z. Guo (2019), Tectonic Evolution of the Pamir Recorded in the Western Tarim Basin (China): Sedimentologic and Magnetostratigraphic Analyses of the Aertashi Section, *Tectonics*, *38*(2), 492-515.

Cao, K., G.-C. Wang, M. Bernet, P. van der Beek, and K.-X. Zhang (2015), Exhumation history of the West Kunlun Mountains, northwestern Tibet: Evidence for a long-lived, rejuvenated orogen, *Earth and Planetary Science Letters*, *432*, 391-403.

Chang, J., S. Glorie, N. Qiu, K. Min, Y. Xiao, and W. Xu (2021), Late Miocene (10.0∼6.0 Ma) Rapid Exhumation of the Chinese South Tianshan: Implications for the Timing of Aridification in the Tarim Basin, *Geophysical Research Letters*, *48*(3), e2020GL090623.

Charreau, J., S. Gilder, Y. Chen, S. Dominguez, J.-P. Avouac, S. Sen, M. Jolivet, Y. Li, and W. Wang (2006), Magnetostratigraphy of the Yaha section, Tarim Basin (China): 11 Ma acceleration in erosion and uplift of the Tian Shan mountains, *Geology*, *34*(3), 181-184.

Charreau, J., A. Sartégou, D. Saint-Carlier, J. Lavé, P.-H. Blard, S. Dominguez, S. L. Wang, G. Rao, and A. Team (2020), Late Miocene to Quaternary slip history across the Qiulitag anticline in the southern Tianshan piedmont, *Terra Nova*, *32*(1), 89-96.

Charreau, J., C. Gumiaux, J.-P. Avouac, R. Augier, Y. Chen, L. Barrier, S. Gilder, S. Dominguez, N. Charles, and Q. Wang (2009), The Neogene Xiyu Formation, a diachronous prograding gravel wedge at front of the Tianshan: Climatic and tectonic implications, *Earth and Planetary Science Letters*, *287*(3-4), 298-310.

Chen, H., Y. Zhang, X. Cheng, X. Lin, H. Deng, X. Shi, Y. Li, H. Wu, C. Li, and S. Yang (2022), Using migrating growth strata to confirm a ∼230-km-long detachment thrust in the southern Tarim Basin, *Journal of Structural Geology*, *154*, 104488.

Chen, H. L., K. Li, Y. Li, H. X. Wu, X. G. Cheng, C. M. Zeng, J. Shi, and Y. Q. Zhang (2018), The segmentation deformation of the thrust belt in front of Western Kunlun, western China, and its controlling factors, *Acta Petrol Sin*, *34*(7), 1933-1942.

Chen, J., D. W. Burbank, K. M. Scharer, E. Sobel, J. Yin, C. Rubin, and R. Zhao (2002), Magnetochronology of the Upper Cenozoic strata in the Southwestern Chinese Tian Shan: rates of Pleistocene folding and thrusting, *Earth and Planetary Science Letters*, *195*(1-2), 113-130.

Cheng, X., H. Chen, X. Lin, L. Wu, and J. Gong (2017), Geometry and kinematic evolution of the Hotan-Tiklik segment of the western Kunlun thrust belt: Constrained by structural analyses and apatite fission track thermochronology, *The Journal of Geology*, *125*(1), 65-82.

Cowgill, E., A. Yin, T. M. Harrison, and W. Xiao-Feng (2003), Reconstruction of the Altyn Tagh fault based on U-Pb geochronology: Role of back thrusts, mantle sutures, and heterogeneous crustal strength in forming the Tibetan Plateau, *Journal of Geophysical Research: Solid Earth*, *108*(B7).

England, P., and G. Houseman (1989), Extension during continental convergence, with application to the Tibetan Plateau, *Journal of Geophysical Research*, *94*(B12), 17561-17579.

Ford, M., E. A. Williams, A. Artoni, J. Vergés, and S. Hardy (1997), Progressive evolution of a fault-related fold pair from growth strata geometries, Sant Llorenç de Morunys, SE Pyrenees, *Journal of Structural Geology*, *19*(3-4), 413-441.

Guilbaud, C., M. Simoes, L. Barrier, A. Laborde, J. Van der Woerd, H. Li, P. Tapponnier, T. Coudroy, and A. Murray (2017), Kinematics of Active Deformation Across the Western Kunlun Mountain Range (Xinjiang, China) and Potential Seismic Hazards Within the

939 Southern Tarim Basin, *Journal of Geophysical Research: Solid Earth*, *122*(12), 10,398-
940 310,426.
941 Hardy, S., and J. Poblet (1994), Geometric and numerical model of progressive limb rotation
942 in detachment folds, *Geology*, *22*(4), 371-374.
943 Heermance, R. V., J. Chen, D. W. Burbank, and C. Wang (2007), Chronology and tectonic
944 controls of Late Tertiary deposition in the southwestern Tian Shan foreland, NW China,
945 *Basin Research*, *19*(4), 599-632.
946 Heermance, R. V., J. Chen, D. W. Burbank, and J. Miao (2008), Temporal constraints and
947 pulsed Late Cenozoic deformation during the structural disruption of the active Kashi
948 foreland, northwest China, *Tectonics*, *27*(6), n/a-n/a.
949 Huang, B., J. D. A. Piper, Q. Qiao, H. Wang, and C. Zhang (2010), Magnetostratigraphic and
950 rock magnetic study of the Neogene upper Yaha section, Kuche Depression (Tarim Basin):
951 Implications to formation of the Xiyu conglomerate formation, NW China, *Journal of*
952 *Geophysical Research*, *115*(B1).
953 Huang, B., J. D. A. Piper, S. Peng, T. Liu, Z. Li, Q. Wang, and R. Zhu (2006),
954 Magnetostratigraphic study of the Kuche Depression, Tarim Basin, and Cenozoic uplift of the
955 Tian Shan range, western China, *Earth and Planetary Science Letters*, *251*(3–4), 346-364.
956 Hubbard, J., and J. H. Shaw (2009), Uplift of the Longmen Shan and Tibetan plateau, and
957 the 2008 Wenchuan (M = 7.9) earthquake, *Nature*, *458*, 194-197.
958 Hubert-Ferrari, A., J. Suppe, R. Gonzalez-Mieres, and X. Wang (2007), Mechanisms of
959 active folding of the landscape (southern Tian Shan, China), *Journal of Geophysical*
960 *Research*, *112*(B3).
961 Jarvis, A., H. I. Reuter, A. Nelson, and E. Guevara (2008), Hole-filled SRTM for the globe
962 Version 4, *available from the CGIAR-CSI SRTM 90m Database (http://srtm.csi.cgiar.org)*, *15*,
963 25-54.
964 Jiang, X.-D., and Z.-X. Li (2014), Seismic reflection data support episodic and simultaneous
965 growth of the Tibetan Plateau since 25 Myr, *Nat Commun*, *5*(1), 5453.
966 Jiang, X.-D., Z.-X. Li, and H. Li (2013), Uplift of the West Kunlun Range, northern Tibetan
967 Plateau, dominated by brittle thickening of the upper crust, *Geology*, *41*(4), 439-442.
968 Jiang, Z., S. Jiang, X. Lan, B. Wang, S. Huang, and H. Zhang (2018), Neotectonic evolution
969 of the Tarim Basin Craton from Neogene to quaternary, *International Geology Review*,
970 *60*(10), 1213-1230.
971 Kapp, P., and P. G. DeCelles (2019), Mesozoic-Cenozoic geological evolution of the
972 Himalayan-Tibetan orogen and working tectonic hypotheses, *American Journal of Science*,
973 *319*(3), 159-254.
974 Laborde, A., L. Barrier, M. Simoes, H. Li, T. Coudroy, J. Van der Woerd, and P. Tapponnier
975 (2019), Cenozoic deformation of the Tarim Basin and surrounding ranges (Xinjiang, China):
976 A regional overview, *Earth-Science Reviews*, *197*, 102891.
977 Li, C., S. Wang, and L. Wang (2019), Tectonostratigraphic history of the southern Tian Shan,
978 western China, from seismic reflection profiling, *Journal of Asian Earth Sciences*, *172*, 101-
979 114.
980 Li, C., et al. (2021), Cenozoic basin-filling evolution of the SW Tarim Basin and its
981 implications for the uplift of western Kunlun: Insights from (seismo)stratigraphy,
982 *Palaeogeography, Palaeoclimatology, Palaeoecology*, *562*, 110149.
983 Li, G., M. Sandiford, A. Fang, B. Kohn, D. Sandiford, B. Fu, T. Zhang, Y. Cao, and F. Chen
984 (2019), Multi-stage exhumation history of the West Kunlun orogen and the amalgamation of
985 the Tibetan Plateau, *Earth and Planetary Science Letters*, *528*, 115833.
986 Li, T., J. Chen, L. Fang, Z. Chen, J. A. Thompson, and C. Jia (2016), The 2015Mw 6.4
987 Pishan Earthquake: Seismic Hazards of an Active Blind Wedge Thrust System at the
988 Western Kunlun Range Front, Northwest Tibetan Plateau, *Seismological Research Letters*,
989 *87*(3), 601-608.
990 Li, Y.-J., L. Wen, H.-L. Li, G.-X. Peng, B. Qiu, D.-M. Zheng, J.-C. Luo, Q. Zhang, and T.-G.
991 Jia (2016a), The Madong Early Paleozoic fold–thrust belt in southern Tarim Basin, *Journal of*
992 *Asian Earth Sciences*, *115*, 247-256.

Li, Y.-J., et al. (2016b), Cenozoic faults and faulting phases in the western Tarim Basin (NW China): Effects of the collisions on the southern margin of the Eurasian Plate, *Journal of Asian Earth Sciences*, *132*, 40-57.
Lu, R., X. Xu, D. He, B. Liu, X. Tan, and X. Wang (2016), Coseismic and blind fault of the 2015 Pishan Mw 6.5 earthquake: Implications for the sedimentary-tectonic framework of the western Kunlun Mountains, northern Tibetan Plateau, *Tectonics*, *35*(4), 956-964.
Lyon-Caen, H., and P. Molnar (1984), Gravity anomalies and the structure of western Tibet and the Southern Tarim Basin, *Geophysical Research Letters*, *11*(12), 1251-1254.
Matte, P., P. Tapponnier, N. Arnaud, L. Bourjot, J. P. Avouac, P. Vidal, L. Qing, Y. S. Pan, and W. Yi (1996), Tectonics of Western Tibet, between the Tarim and the Indus, *Earth and Planetary Science Letters*, *142*(3-4), 311-&.
Medwedeff, D. A. (1989), Growth Fault-Bend Folding at Southeast Lost Hills, San Joaquin Valley, California, *AAPG Bulletin*, *73*(1), 54-67.
Mériaux, A. S., F. J. Ryerson, P. Tapponnier, J. Van der Woerd, R. C. Finkel, X. Xu, Z. Xu, and M. W. Caffee (2004), Rapid slip along the central Altyn Tagh Fault: morphochronologic evidence from Cherchen He and Sulamu Tagh, *Journal of Geophysical Research: Solid Earth*, *109*(B6).
Métivier, F., and Y. Gaudemer (1997), Mass transfer between eastern Tien Shan and adjacent basins (central Asia): Constraints on regional tectonics and topography, *Geophysical Journal International*, *128*(1), 1-17.
Molnar, P., and J. M. Stock (2009), Slowing of India's convergence with Eurasia since 20 Ma and its implications for Tibetan mantle dynamics, *Tectonics*, *28*(3), n/a-n/a.
Patriat, P., and J. Achache (1984), India–Eurasia collision chronology has implications for crustal shortening and driving mechanism of plates, *Nature*, *311*(5987), 615-621.
Phillips, R. J., and M. P. Searle (2007), Macrostructural and microstructural architecture of the Karakoram fault: Relationship between magmatism and strike-slip faulting, *Tectonics*, *26*(3), n/a-n/a.
Poblet, J., M. Bulnes, K. McClay, and S. Hardy (2004), Plots of crestal structural relief and fold area versus shortening—A graphical technique to unravel the kinematics of thrust-related folds, in *Thrust Tectonics and Hydrocarbon Systems, Memoir 82*, edited by K. R. McClay, pp. 372-399, American Association of Petroleum Geologists, Tulsa.
Riba, O. (1976), Syntectonic unconformities of the Alto Cardener, Spanish Pyrenees: a genetic interpretation, *Sedimentary Geology*, *15*(3), 213-233.
Royden, L. H., B. C. Burchfiel, R. W. King, E. Wang, Z. Chen, F. Shen, and Y. Liu (1997), Surface Deformation and Lower Crustal Flow in Eastern Tibet, *Science*, *276*(5313), 788-790.
Shaw, J. H., C. Connors, and J. Suppe (2005), *Seismic interpretation of contractional fault-related folds: An AAPG seismic atlas*, American Association of Petroleum Geologists
Sobel, E. R., and T. A. Dumitru (1997), Thrusting and exhumation around the margins of the western Tarim basin during the India-Asia collision, *Journal of Geophysical Research: Solid Earth*, *102*(B3), 5043-5063.
Song, Z., L. Tang, and C. Liu (2021), Variations of thick-skinned deformation along tumuxiuke thrust in Bachu uplift of Tarim Basin, northwestern China, *Journal of Structural Geology*, *144*, 104277.
Sun, J., Y. Li, Z. Zhang, and B. Fu (2009), Magnetostratigraphic data on Neogene growth folding in the foreland basin of the southern Tianshan Mountains, *Geology*, *37*(11), 1051-1054.
Sun, T., J. Qi, Q. Ni, P. Ma, C. Han, Q. Li, and P. Gong (2019), The influence of syntectonic sedimentation on thrust belt deformation: a kinematic model example from the triangle zone within the Western Kunlun thrust belt, *Int J Earth Sci*, *108*, 1121-1136.
Suppe, J., G. T. Chou, and S. C. Hook (1992), Rates of folding and faulting determined from growth strata, in *Thrust Tectonics*, edited by K. R. McClay, pp. 105-121, Springer Dordrecht.
Tapponnier, P., and P. Molnar (1977), Active Faulting and Tectonics in China, *Journal of Geophysical Research*, *82*(20), 2905-2930.

Tapponnier, P., X. Zhiqin, F. Roger, B. Meyer, N. Arnaud, G. Wittlinger, and Y. Jingsui (2001), Oblique stepwise rise and growth of the Tibet plateau, *Science*, *294*(5547), 1671-1677.
Thompson, J. A., D. W. Burbank, T. Li, J. Chen, and B. Bookhagen (2015), Late Miocene northward propagation of the northeast Pamir thrust system, northwest China, *Tectonics*, *34*(3), 510-534.
Thompson Jobe, J. A., T. Li, B. Bookhagen, J. Chen, and D. Burbank (2018), Dating growth strata and basin fill by combining 26Al/10Be burial dating and magnetostratigraphy: Constraining active deformation in the Pamir–Tian Shan convergence zone, NW China, *Lithosphere*, *10*(6), 806-828.
Tong, D., J. Zhang, H. Yang, D. Hu, and J. Ren (2012), Fault system, deformation style and development mechanism of the Bachu uplift, Tarim basin, *Journal of Earth Science*, *23*(4), 529-541.
Valli, F., et al. (2008), New U-Th/Pb constraints on timing of shearing and long-term slip-rate on the Karakorum fault, *Tectonics*, *27*(5).
Vergés, J., M. Marzo, and J. A. Muñoz (2002), Growth strata in foreland settings, *Sedimentary geology*, *146*(1-2), 1-9.
Wang, C.-Y., H.-L. Chen, X.-G. Cheng, and K. Li (2013), Evaluating the role of syn-thrusting sedimentation and interaction with frictional detachment in the structural evolution of the SW Tarim basin, NW China: Insights from analogue modeling, *Tectonophysics*, *608*, 642-652.
Wang, C., X.-G. Cheng, H.-L. Chen, K. Li, X.-G. Fan, and C.-Y. Wang (2016), From folding to transpressional faulting: the Cenozoic Fusha structural belt in front of the Western Kunlun Orogen, northwestern Tibetan Plateau, *International Journal of Earth Sciences*, *105*(5), 1621-1636.
Wang, E., J. Wan, and J. Liu (2003), Late Cenozoic geological evolution of the foreland basin bordering the West Kunlun range in Pulu area: Constraints on timing of uplift of northern margin of the Tibetan Plateau, *Journal of Geophysical Research: Solid Earth*, *108*(B8).
Wang, S., Y. Chen, J. Charreau, Y. Li, Z. Chen, G. Zhu, H. Xu, C. Li, and L. Wang (2021), Underthrusting of the Tarim Lithosphere Beneath the Western Kunlun Range, Insights From Seismic Profiling Evidence, *Tectonics*, *40*(2), e2019TC005932.
Wittlinger, G., J. Vergne, P. Tapponnier, V. Farra, G. Poupinet, M. Jiang, H. Su, G. Herquel, and A. Paul (2004), Teleseismic imaging of subducting lithosphere and Moho offsets beneath western Tibet, *Earth and Planetary Science Letters*, *221*(1-4), 117-130.
Xu, J., J. Chen, J. R. Arrowsmith, T. Li, B. Zhang, N. Di, and W. Pang (2020), Growth Model and Tectonic Significance of the Guman Fold Along the Western Kunlun Mountain Front (Xinjiang, China) Derived From Terrace Deformation and Seismic Data, *Frontiers in Earth Science*, *8*, 590043.
Yang, H. J., Y. Li, X. Feng, M. Z. Zheng, C. J., and Y. Zhao (2007), Analysis of thrustings of the Mazarthage structural belt in the Tarim Basin *Chinese Journal of Geology*(1-12).
Yang, Y., J. Z. Hu, and C. S. Lin (2009), Geological structure and petroleum geology features of Aqike anticline in southwest Tarim Basin, *Acta Geosci. Sin*, *30*, 263-270.
Zhang, P. Z., P. Molnar, and X. Xu (2007), Late Quaternary and present-day rates of slip along the Altyn Tagh Fault, northern margin of the Tibetan Plateau, *Tectonics*, *26*(5), TC5010.
Zhang, T., X. Fang, C. Song, E. Appel, and Y. Wang (2014), Cenozoic tectonic deformation and uplift of the South Tian Shan: Implications from magnetostratigraphy and balanced cross-section restoration of the Kuqa depression, *Tectonophysics*, *628*, 172-187.
Zheng, H., X. Wei, R. Tada, P. D. Clift, B. Wang, F. Jourdan, P. Wang, and M. He (2015), Late oligocene–early miocene birth of the Taklimakan Desert, *Proceedings of the National Academy of Sciences*, *112*(25), 7662-7667.

Figure 1.

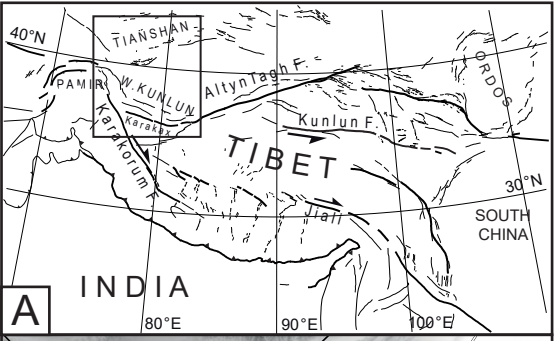
A
TIANSHAN
PAMIR
W.KUNLUN
Karakax
Altyn Tagh F.
Karakorum
Kunlun F.
TIBET
ORDOS
30°N
SOUTH CHINA
Jiali
INDIA
80°E
90°E
100°E
40°N

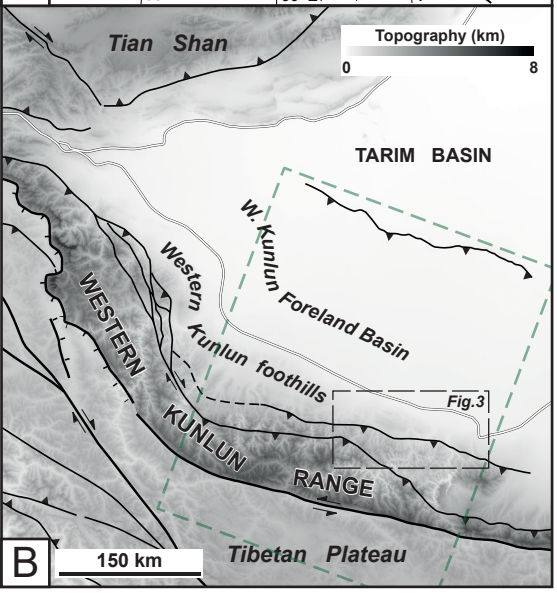
B
Tian Shan
Topography (km)
0
8
TARIM BASIN
W. Kunlun Foreland Basin
Western Kunlun foothills
WESTERN KUNLUN RANGE
Fig.3
150 km
Tibetan Plateau

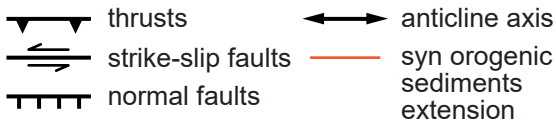
thrusts
strike-slip faults
normal faults
anticline axis
syn orogenic sediments extension

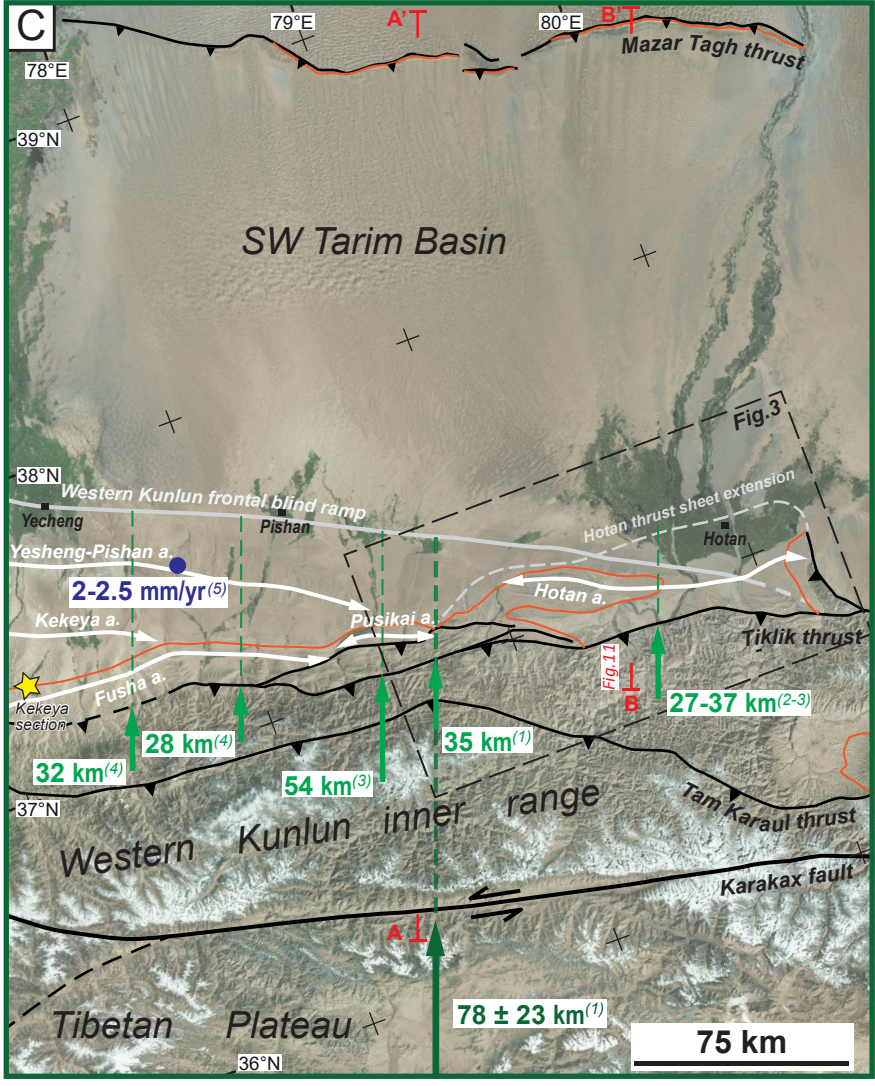
C
79°E
A'
80°E
B'
Mazar Tagh thrust
78°E
39°N
SW Tarim Basin
Fig.3
38°N
Western Kunlun frontal blind ramp
Yecheng
Pishan
Yesheng-Pishan a.
2-2.5 mm/yr(5)
Kekeya a.
Pusikai a.
Hotan thrust sheet extension
Hotan
Hotan a.
Tiklik thrust
Fig.11
B
27-37 km(2-3)
Kekeya section
Fusha a.
28 km(4)
32 km(4)
54 km(3)
35 km(1)
37°N
Western Kunlun inner range
Tam Karaul thrust
Karakax fault
A
Tibetan Plateau
78 ± 23 km(1)
75 km
36°N

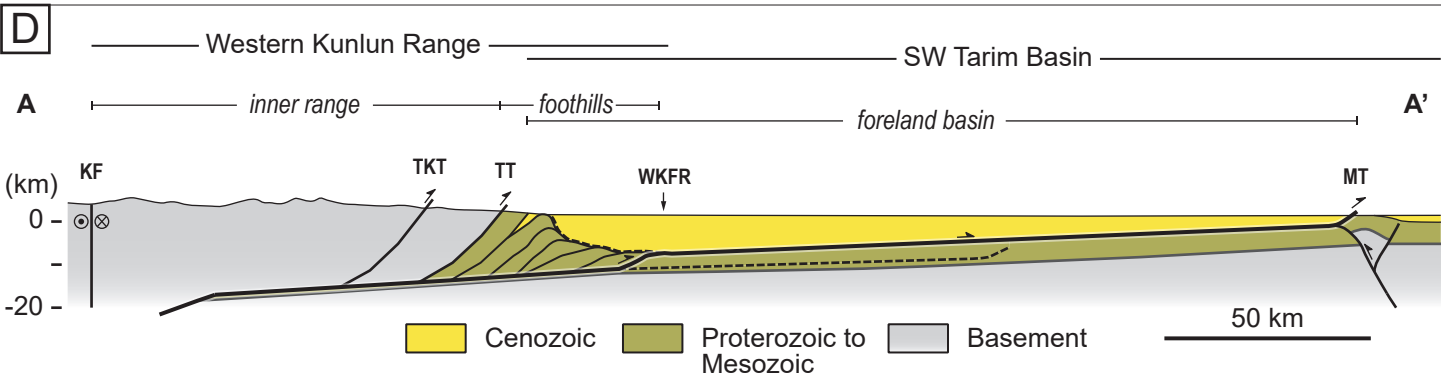
D
Western Kunlun Range
SW Tarim Basin
A
inner range
foothills
foreland basin
A'
(km)
KF
TKT
TT
WKFR
MT
0
-20
50 km
Cenozoic
Proterozoic to Mesozoic
Basement

Figure 2.

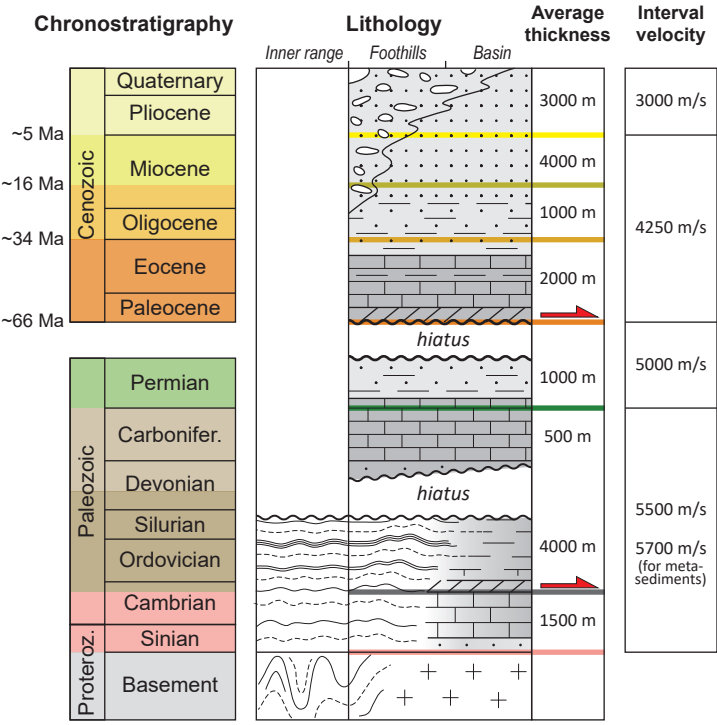

Seismic horizons

- Base Pliocene (T3)
- Base Mid. Miocene (T5)
- Base Oligocene (T6)
- Base Paleocene (T8)
- Base Permian (Tg2)
- Base Upp. Cambrian
- Base Sinian
- Detachment levels

Lithologies

- Conglomerates
- Sandstones
- Shales
- Limestones
- Evaporites
- Marine deposits
- Continental deposits
- Meta-sediments
- Metamorphic rocks
- Igneous rocks
- Major unconformities

Figure 3.

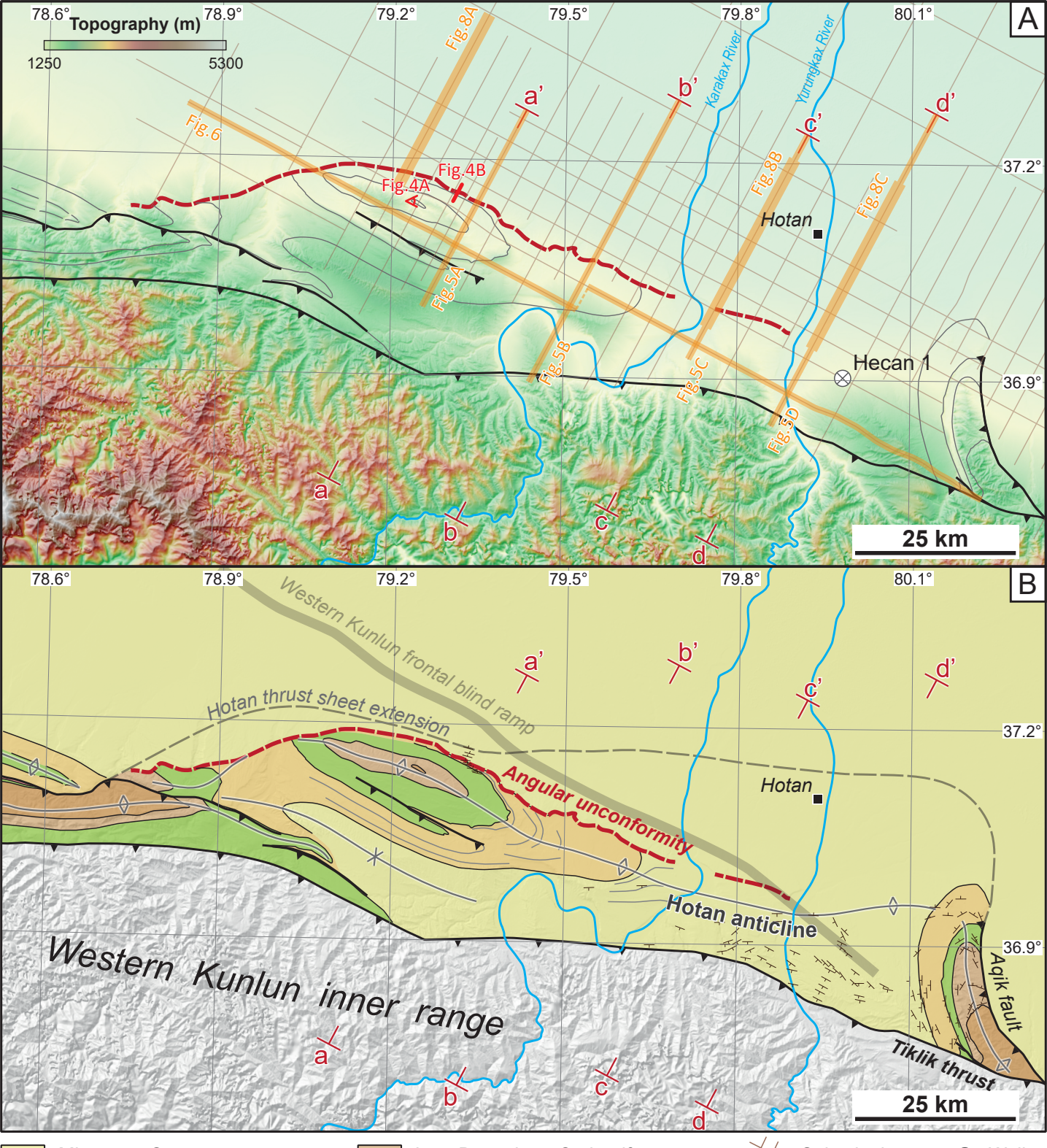
A
B
78.6°
78.9°
79.2°
79.5°
79.8°
80.1°
Topography (m)
1250
5300
Fig.8A
Fig.6
Fig.4A
Fig.4B
Fig.5A
Fig.5B
Fig.5C
Fig.5D
Fig.8B
Fig.8C
a'
b'
c'
d'
Karakax River
Yurungkax River
Hotan
Hecan 1
37.2°
36.9°
a
b
c
d
25 km
Western Kunlun frontal blind ramp
Hotan thrust sheet extension
Angular unconformity
Hotan anticline
Aqik fault
Tiklik thrust
Western Kunlun inner range
Miocene - Quaternary
Paleocene - Lower Miocene
Permian
Late Devonian - Carboniferous
Ordovician - Silurian
Proterozoic - Paleozoic undiff.
Seismic dataset
Wells
Balanced cross-sections
(Figure 7)

Figure 4.

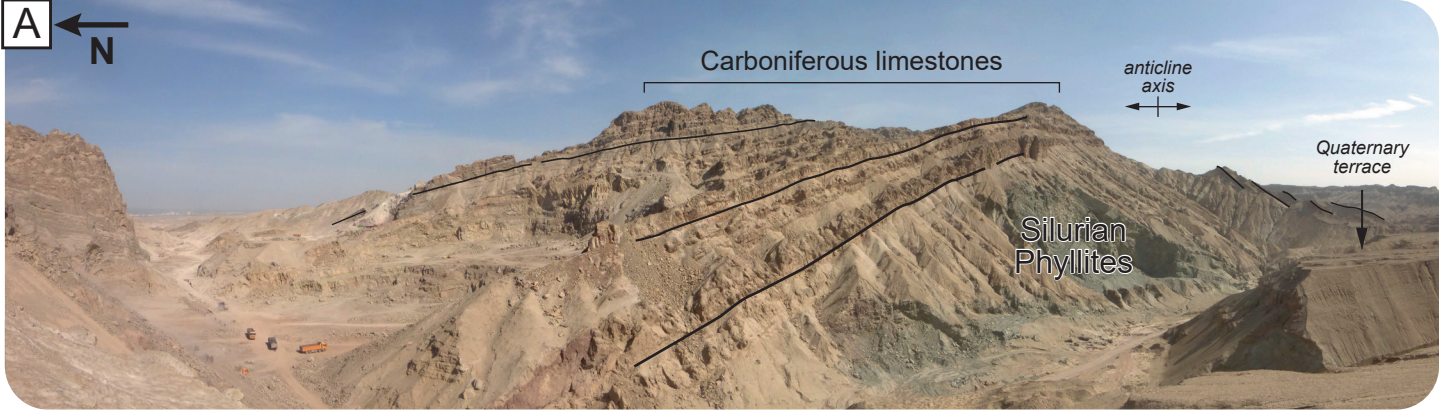
A
N
Carboniferous limestones
anticline axis
Quaternary terrace
Silurian Phyllites

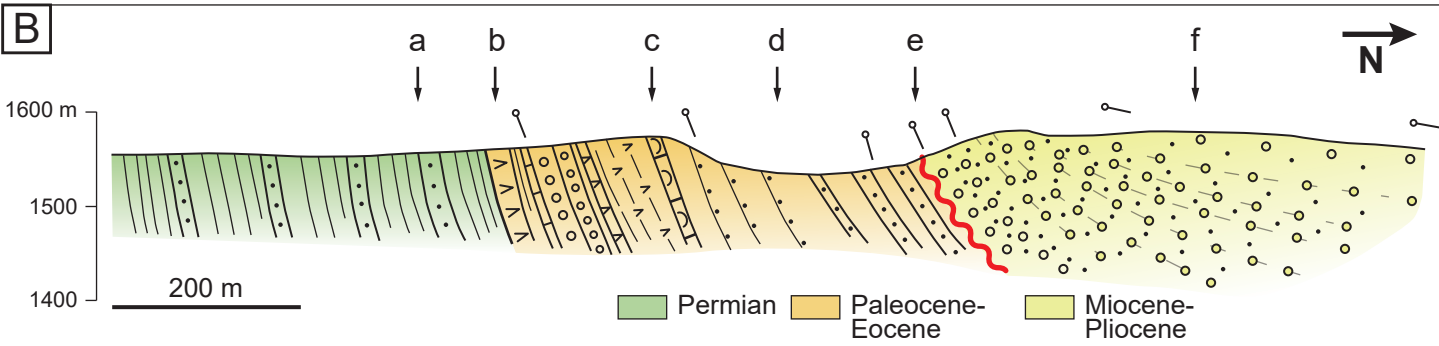
B
a
b
c
d
e
f
N
1600 m
1500
1400
200 m
Permian
Paleocene-Eocene
Miocene-Pliocene

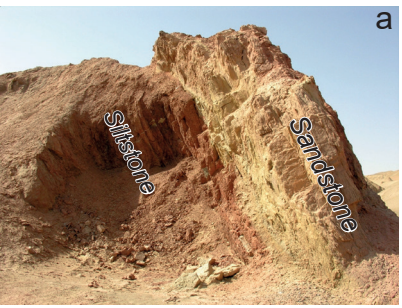
a
Siltstone
Sandstone

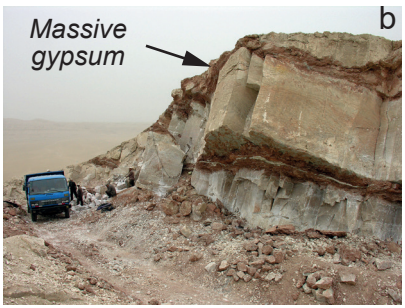
b
Massive gypsum

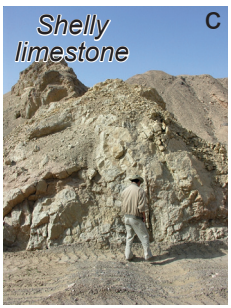
c
Shelly limestone


d
Sandstone/ siltstone

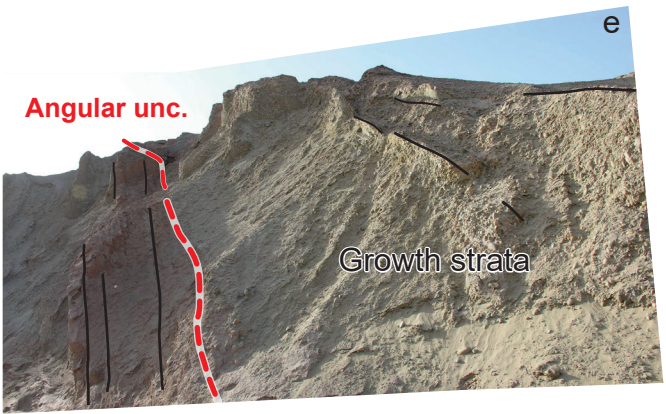
e
Angular unc.
Growth strata

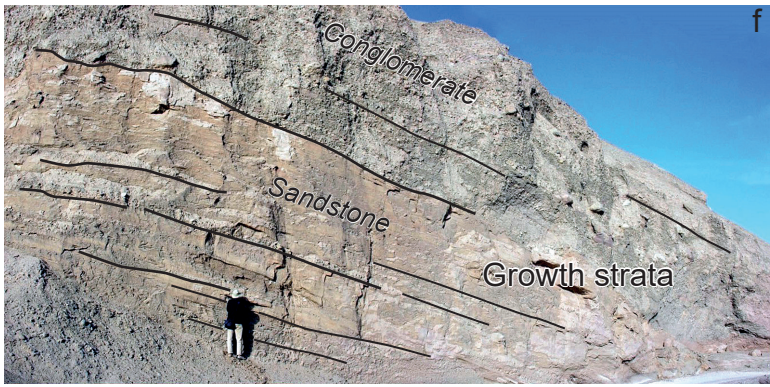
f
Conglomerate
Sandstone
Growth strata

Figure 5.

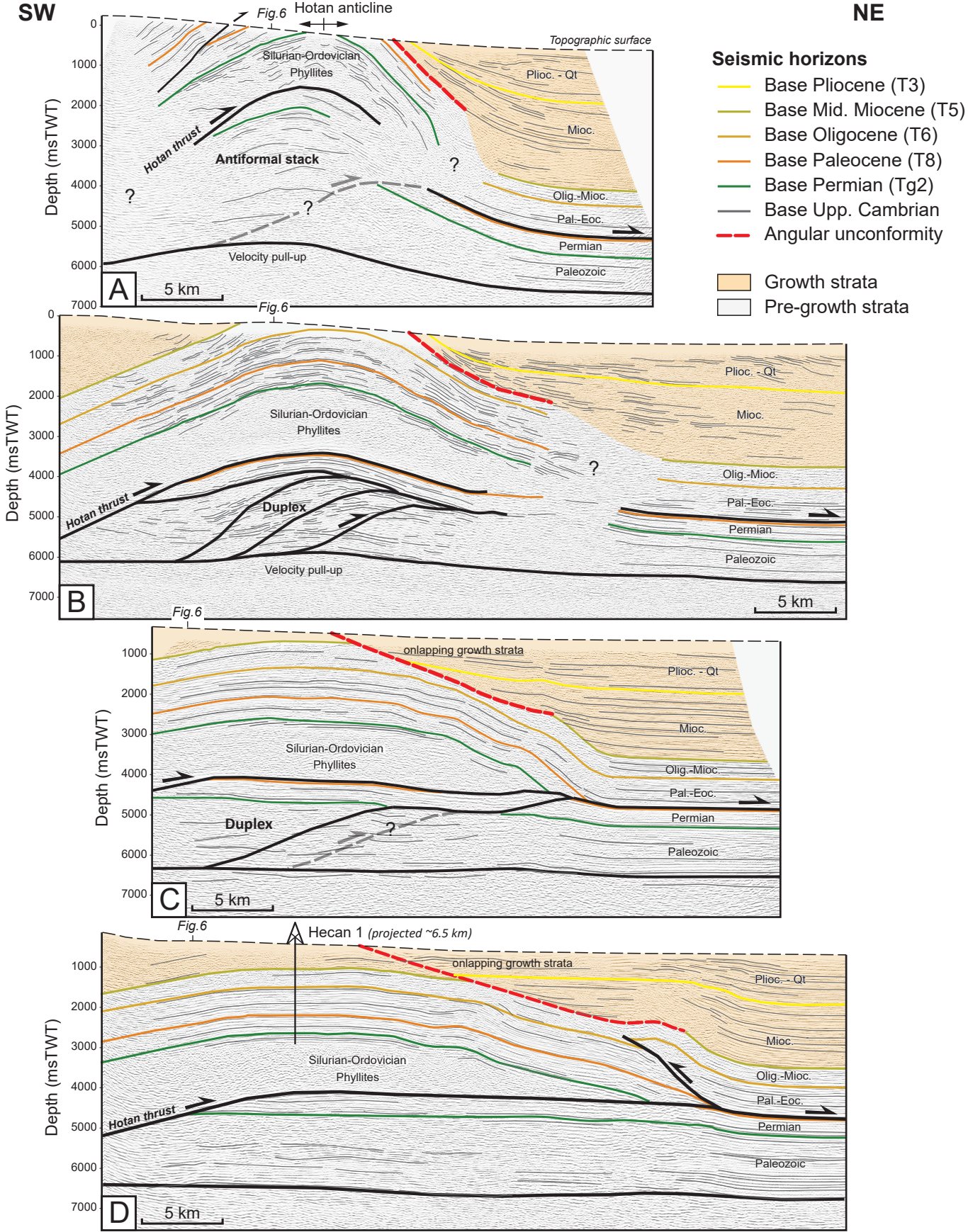
SW
NE
Fig.6
Hotan anticline
Topographic surface
Silurian-Ordovician
Phyllites
Plioc. - Qt
Mioc.
Olig.-Mioc.
Pal.-Eoc.
Permian
Paleozoic
Hotan thrust
Antiformal stack
Velocity pull-up
Depth (msTWT)
A
5 km
Duplex
B
onlapping growth strata
C
Hecan 1 (projected ~6.5 km)
D
Seismic horizons
Base Pliocene (T3)
Base Mid. Miocene (T5)
Base Oligocene (T6)
Base Paleocene (T8)
Base Permian (Tg2)
Base Upp. Cambrian
Angular unconformity
Growth strata
Pre-growth strata

Figure 6.

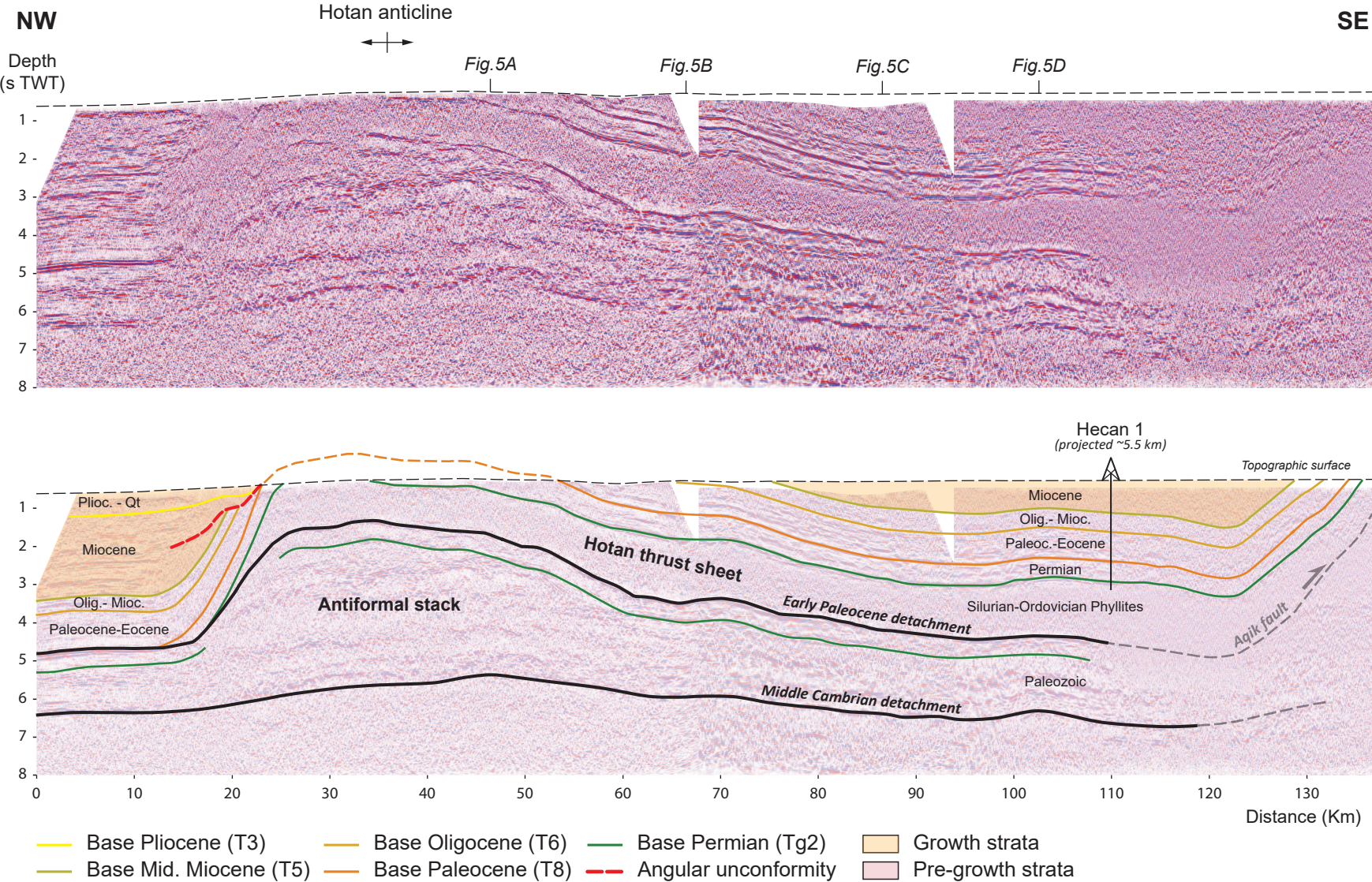
NW
SE
Hotan anticline
Depth
(s TWT)
Fig.5A
Fig.5B
Fig.5C
Fig.5D
Hecan 1
(projected ~5.5 km)
Topographic surface
Plioc. - Qt
Miocene
Olig.- Mioc.
Paleocene-Eocene
Antiformal stack
Hotan thrust sheet
Early Paleocene detachment
Middle Cambrian detachment
Aqik fault
Miocene
Olig.- Mioc.
Paleoc.-Eocene
Permian
Silurian-Ordovician Phyllites
Paleozoic
Distance (Km)
Base Pliocene (T3)
Base Mid. Miocene (T5)
Base Oligocene (T6)
Base Paleocene (T8)
Base Permian (Tg2)
Angular unconformity
Growth strata
Pre-growth strata

Figure 7.

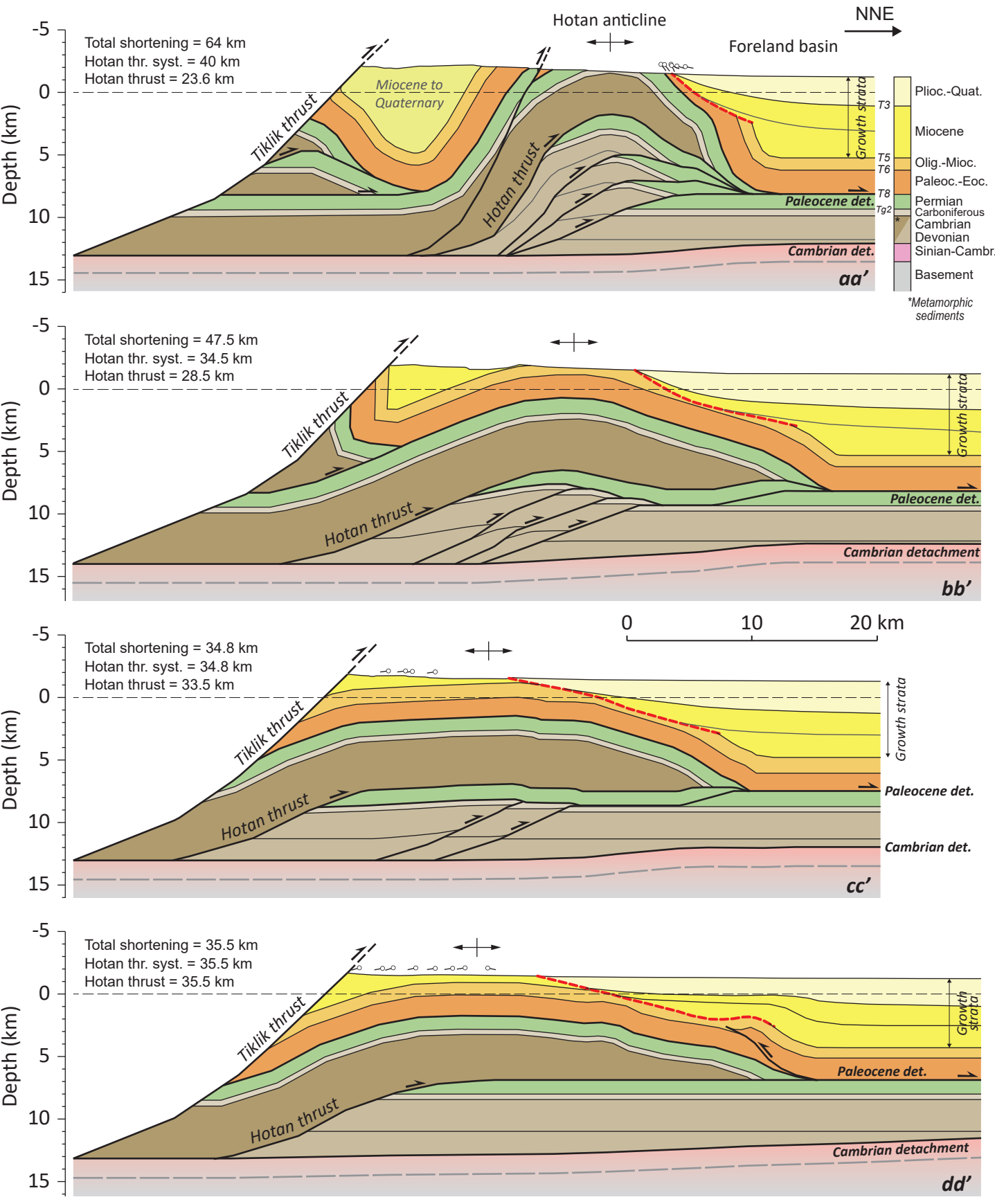
Hotan anticline
NNE
Foreland basin
Total shortening = 64 km
Hotan thr. syst. = 40 km
Hotan thrust = 23.6 km
Miocene to Quaternary
Tiklik thrust
Hotan thrust
Growth strata
T3
T5
T6
T8
Tg2
Paleocene det.
Cambrian det.
aa'
Plioc.-Quat.
Miocene
Olig.-Mioc.
Paleoc.-Eoc.
Permian
Carboniferous
Cambrian
Devonian
Sinian-Cambr.
Basement
*Metamorphic sediments
Depth (km)
-5
0
5
10
15
Total shortening = 47.5 km
Hotan thr. syst. = 34.5 km
Hotan thrust = 28.5 km
Tiklik thrust
Hotan thrust
Growth strata
Paleocene det.
Cambrian detachment
bb'
0
10
20 km
Total shortening = 34.8 km
Hotan thr. syst. = 34.8 km
Hotan thrust = 33.5 km
Tiklik thrust
Hotan thrust
Growth strata
Paleocene det.
Cambrian det.
cc'
Total shortening = 35.5 km
Hotan thr. syst. = 35.5 km
Hotan thrust = 35.5 km
Tiklik thrust
Hotan thrust
Growth strata
Paleocene det.
Cambrian detachment
dd'

Figure 8.

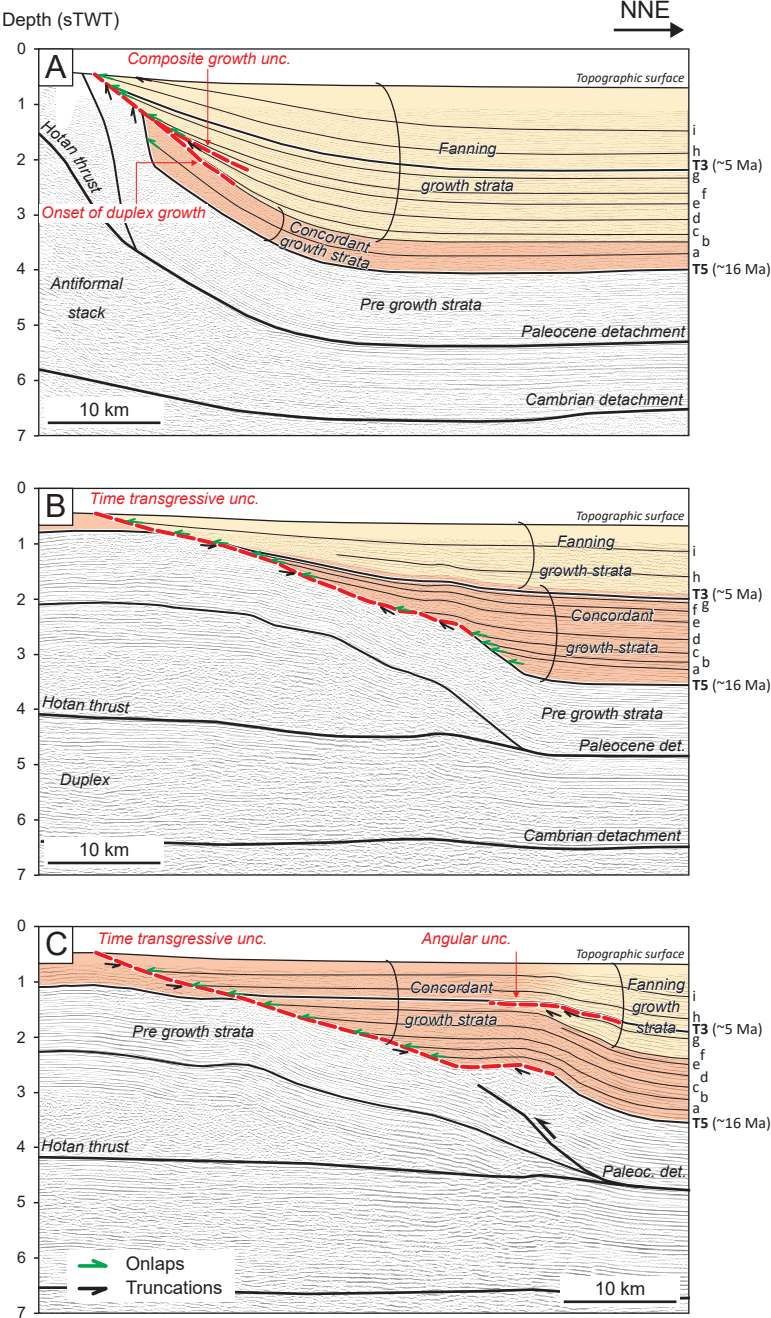
Depth (sTWT)
NNE
A
Composite growth unc.
Topographic surface
Hotan thrust
Fanning
growth strata
Onset of duplex growth
Concordant
growth strata
Antiformal
stack
Pre growth strata
Paleocene detachment
Cambrian detachment
10 km
i
h
T3 (~5 Ma)
g
f
e
d
c
b
a
T5 (~16 Ma)
B
Time transgressive unc.
Topographic surface
Fanning
growth strata
Concordant
growth strata
Hotan thrust
Pre growth strata
Paleocene det.
Duplex
Cambrian detachment
10 km
C
Time transgressive unc.
Angular unc.
Topographic surface
Concordant
growth strata
Fanning
growth
strata
Pre growth strata
Hotan thrust
Paleoc. det.
Onlaps
Truncations
10 km

Figure 9.

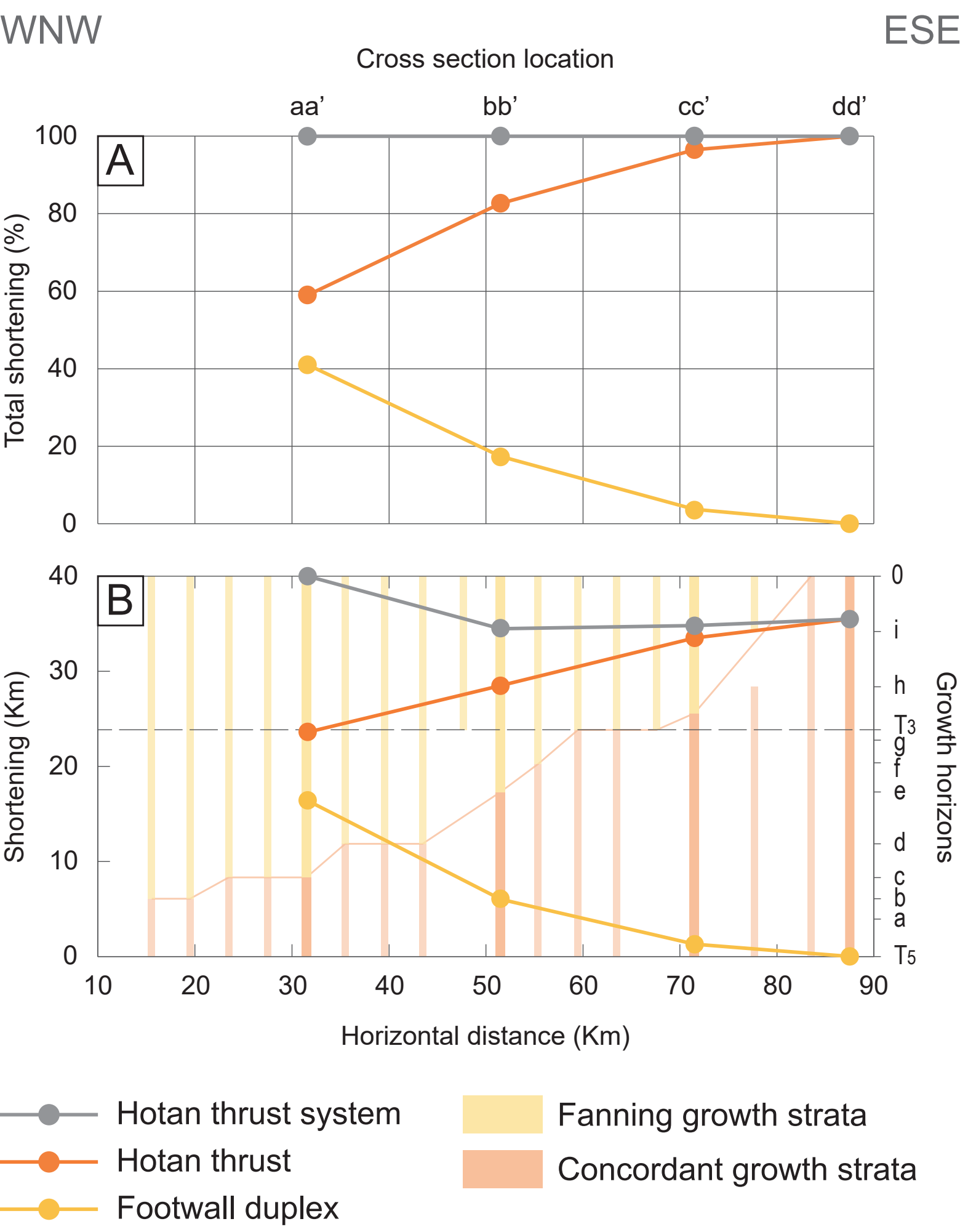
WNW
ESE
Cross section location
aa'
bb'
cc'
dd'
A
Total shortening (%)
100
80
60
40
20
0
B
Shortening (Km)
40
30
20
10
0
0
i
h
T3
g
f
e
d
c
b
a
T5
Growth horizons
10
20
30
40
50
60
70
80
90
Horizontal distance (Km)
Hotan thrust system
Hotan thrust
Footwall duplex
Fanning growth strata
Concordant growth strata

Figure 10.

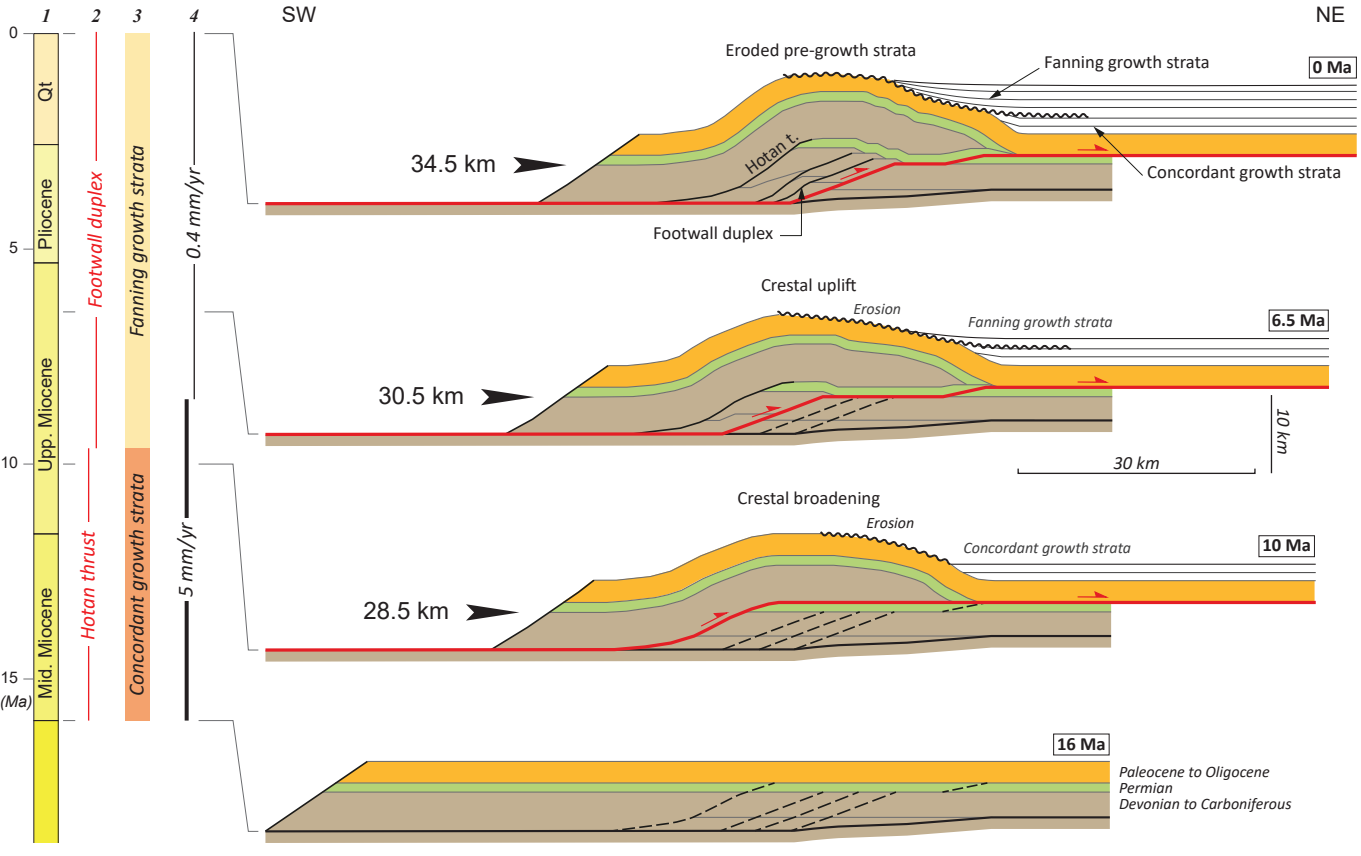
1
2
3
4
SW
NE
0
5
10
15
(Ma)
Qt
Pliocene
Upp. Miocene
Mid. Miocene
Footwall duplex
Hotan thrust
Fanning growth strata
Concordant growth strata
0.4 mm/yr
5 mm/yr
Eroded pre-growth strata
Fanning growth strata
0 Ma
34.5 km
Hotan t.
Concordant growth strata
Footwall duplex
Crestal uplift
Erosion
Fanning growth strata
6.5 Ma
30.5 km
10 km
30 km
Crestal broadening
Erosion
Concordant growth strata
10 Ma
28.5 km
16 Ma
Paleocene to Oligocene
Permian
Devonian to Carboniferous

Figure 11.

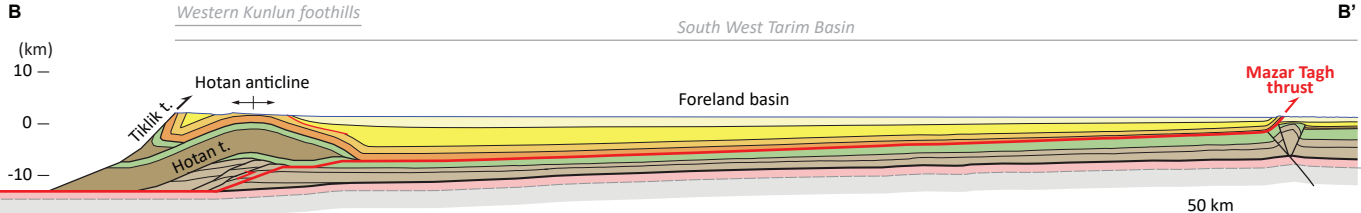
B
B'
Western Kunlun foothills
South West Tarim Basin
(km)
10
0
-10
Hotan anticline
Tiklik t.
Hotan t.
Foreland basin
Mazar Tagh thrust
50 km
Pliocene-Quat.
Miocene
Oligocene-Miocene
Paleocene-Eocene
Permian
Devonian to Carbon.
Sinian-Cambrian
Basement

Figure 12.

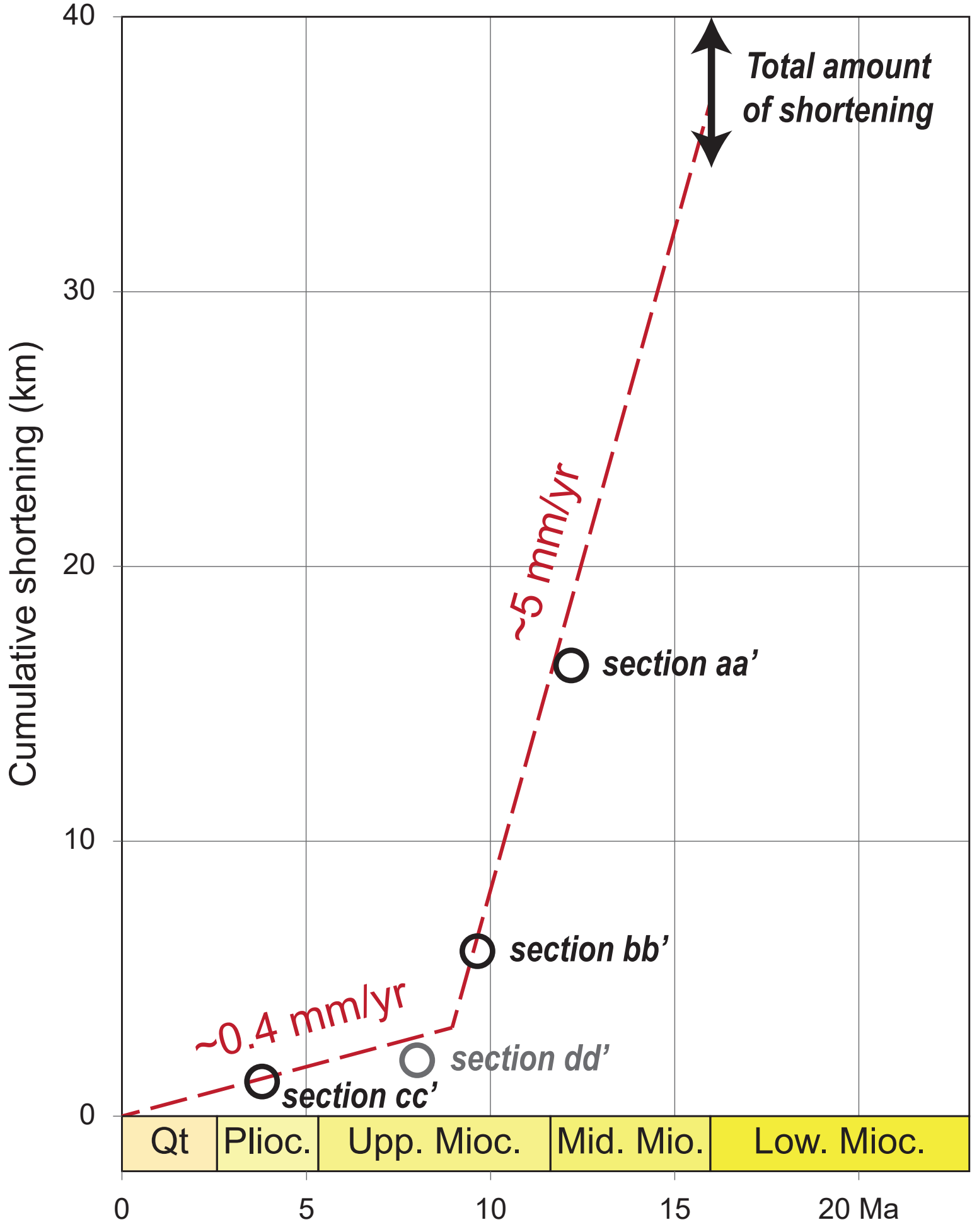
Cumulative shortening (km)
40
30
20
10
0
Total amount
of shortening
~5 mm/yr
section aa'
section bb'
~0.4 mm/yr
section dd'
section cc'
Qt
Plioc.
Upp. Mioc.
Mid. Mio.
Low. Mioc.
0
5
10
15
20 Ma

Figure S1.

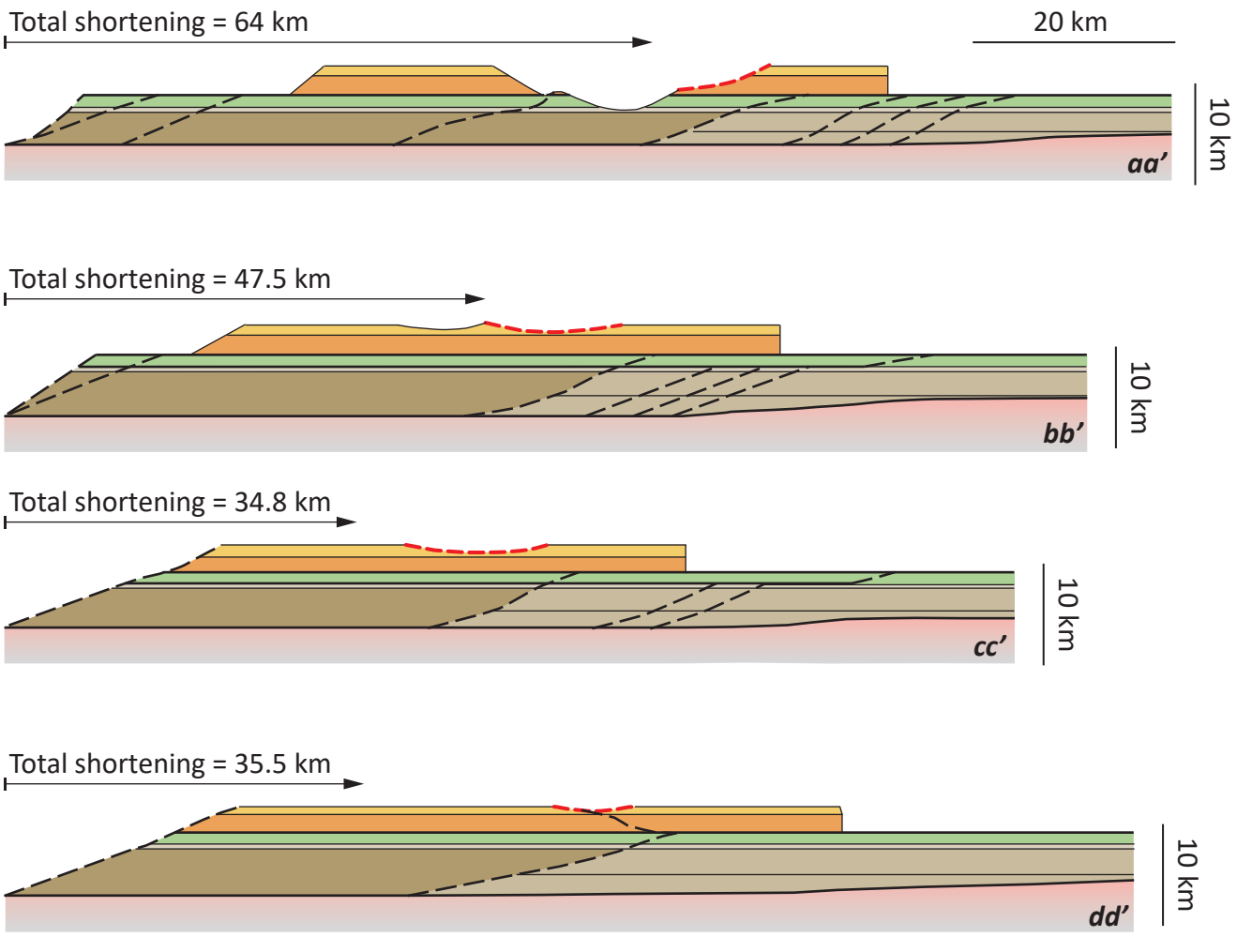
Total shortening = 64 km
20 km
10 km
aa'
Total shortening = 47.5 km
10 km
bb'
Total shortening = 34.8 km
10 km
cc'
Total shortening = 35.5 km
10 km
dd'

Figure S2.

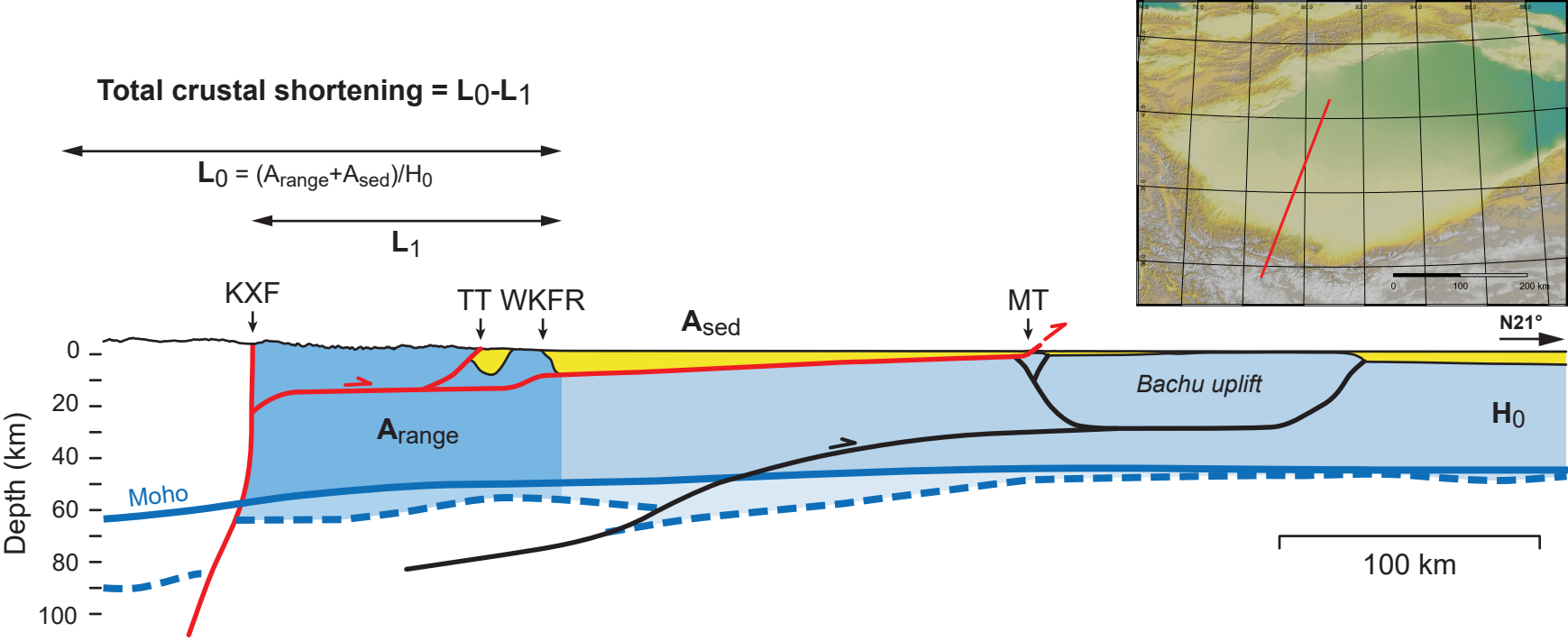
Total crustal shortening = L0-L1
L0 = (Arange+Ased)/H0
L1
KXF
TT WKFR
Ased
MT
N21°
Bachu uplift
Arange
H0
Moho
Depth (km)
0
20
40
60
80
100
100 km
0
100
200 km